The Astrophysical Journal, 979:164 (18pp), 2025 February 1 https://doi.org/10.3847/1538-4357/ad8eba

Discovery and Spectroscopic Confirmation of Aquarius III: A Low-mass Milky Way Satellite Galaxy

W. Cerny[1], A. Chiti[2,3], M. Geha[1], B. Mutlu-Pakdil[4], A. Drlica-Wagner[2,3,5], C. Y. Tan[3,6], M. Adamów[7], A. B. Pace[8,9], J. D. Simon[10], D. J. Sand[11], A. P. Ji[2,3], T. S. Li[12], A. K. Vivas[13], E. F. Bell[14], J. L. Carlin[15], J. A. Carballo-Bello[16], A. Chaturvedi[17], Y. Choi[18], A. Doliva-Dolinsky[4,19], O. Y. Gnedin[14], G. Limberg[3,20,21], C. E. Martínez-Vázquez[22], S. Mau[23,24], G. E. Medina[12], M. Navabi[17], N. E. D. Noël[17], V. M. Placco[18], A. H. Riley[25], I. U. Roederer[26], G. S. Stringfellow[27], C. R. Bom[28], P. S. Ferguson[29], D. J. James[30,31], D. Martínez-Delgado[32,33], P. Massana[34], D. L. Nidever[18,35,36], J. D. Sakowska[17], L. Santana-Silva[28], N. F. Sherman[37], and E. J. Tollerud[38]
(DELVE Collaboration)

[1] Department of Astronomy, Yale University, New Haven, CT 06520, USA; william.cerny@yale.edu
[2] Department of Astronomy and Astrophysics, University of Chicago, Chicago, IL 60637, USA
[3] Kavli Institute for Cosmological Physics, University of Chicago, Chicago, IL 60637, USA
[4] Department of Physics and Astronomy, Dartmouth College, Hanover, NH 03755, USA
[5] Fermi National Accelerator Laboratory, P.O. Box 500, Batavia, IL 60510, USA
[6] Department of Physics, University of Chicago, Chicago, IL 60637, USA
[7] Center for Astrophysical Surveys, National Center for Supercomputing Applications, 1205 West Clark St., Urbana, IL 61801, USA
[8] McWilliams Center for Cosmology, Carnegie Mellon University, 5000 Forbes Avenue, Pittsburgh, PA 15213, USA
[9] Department of Astronomy, University of Virginia, 530 McCormick Road, Charlottesville, VA 22904, USA
[10] Observatories of the Carnegie Institution for Science, 813 Santa Barbara St., Pasadena, CA 91101, USA
[11] Department of Astronomy/Steward Observatory, 933 North Cherry Avenue, Room N204, Tucson, AZ 85721-0065, USA
[12] Department of Astronomy and Astrophysics, University of Toronto, 50 St. George Street, Toronto, ON M5S 3H4, Canada
[13] Cerro Tololo Inter-American Observatory/NSF NOIRLab, Casilla 603, La Serena, Chile
[14] Department of Astronomy, University of Michigan, Ann Arbor, MI 48109, USA
[15] Rubin Observatory/AURA, 950 North Cherry Avenue, Tucson, AZ 85719, USA
[16] Instituto de Alta Investigación, Universidad de Tarapacá, Casilla 7D, Arica, Chile
[17] Department of Physics, University of Surrey, Guildford, GU2 7XH, UK
[18] NSF NOIRLab, 950 N. Cherry Avenue, Tucson, AZ 85719, USA
[19] Department of Chemistry and Physics, University of Tampa, 401 West Kennedy Boulevard, Tampa, FL 33606, USA
[20] Department of Astronomy & Astrophysics, University of Chicago, 5640 S Ellis Avenue, Chicago, IL 60637, USA
[21] Departamento de Astronomia, IAG,Universidade de São Paulo, SP 05508-090, São Paulo, Brazil
[22] International Gemini Observatory/NSF NOIRLab, 670 N. A'ohoku Place, Hilo, HI 96720, USA
[23] Department of Physics, Stanford University, 382 Via Pueblo Mall, Stanford, CA 94305, USA
[24] Kavli Institute for Particle Astrophysics & Cosmology, P.O. Box 2450, Stanford University, Stanford, CA 94305, USA
[25] Institute for Computational Cosmology, Department of Physics, Durham University, South Road, Durham, DH1 3LE, UK
[26] Department of Physics, North Carolina State University, Raleigh, NC 27695, USA
[27] Center for Astrophysics and Space Astronomy, University of Colorado, 389 UCB, Boulder, CO 80309-0389, USA
[28] Centro Brasileiro de Pesquisas Físicas, Rua Dr. Xavier Sigaud 150, 22290-180 Rio de Janeiro, RJ, Brazil
[29] Department of Physics, University of Wisconsin-Madison, Madison, WI 53706, USA
[30] ASTRAVEO LLC, P.O. Box 1668, Gloucester, MA 01931, USA
[31] Applied Materials Inc., 35 Dory Road, Gloucester, MA 01930, USA
[32] Centro de Estudios de Física del Cosmos de Aragón (CEFCA), Unidad Asociada al CSIC, Plaza San Juan 1, 44001 Teruel, Spain
[33] ARAID Foundation, Avda. de Ranillas, 1-D, E-50018 Zaragoza, Spain
[34] NSF NOIRLab, Casilla 603, La Serena, Chile
[35] Department of Physics, Montana State University, P.O. Box 173840, Bozeman, MT 59717-3840, USA
[36] NSF's National Optical-Infrared Astronomy Research Laboratory, 950 N. Cherry Avenue, Tucson, AZ 85719, USA
[37] Institute for Astrophysical Research, Boston University, 725 Commonwealth Avenue, Boston, MA 02215, USA
[38] Space Telescope Science Institute, 3700 San Martin Dr., Baltimore, MD 21218, USA
Received 2024 October 1; accepted 2024 October 20; published 2025 January 23

Abstract

We present the discovery of Aquarius III, an ultra-faint Milky Way satellite galaxy identified in the second data release of the DECam Local Volume Exploration survey. Based on deeper follow-up imaging with DECam, we find that Aquarius III is a low-luminosity ($M_V = -2.5^{+0.3}_{-0.5}$; $L_V = 850^{+380}_{-260}\ L_\odot$), extended ($r_{1/2} = 41^{+9}_{-8}$ pc) stellar system located in the outer halo ($D_\odot = 85 \pm 4$ kpc). From medium-resolution Keck/DEIMOS spectroscopy, we identify 11 member stars and measure a mean heliocentric radial velocity of $v_{\rm sys} = -13.1^{+1.0}_{-0.9}$ km s^{-1} for the system and place an upper limit of $\sigma_v < 3.5$ km s^{-1} ($\sigma_v < 1.6$ km s^{-1}) on its velocity dispersion at the 95% (68%) credible level. Based on calcium-triplet metallicities of the six brightest red giant members, we find that Aquarius III is very metal-poor ([Fe/H]$= -2.61 \pm 0.21$) with a statistically significant metallicity spread

($\sigma_{[Fe/H]} = 0.46^{+0.26}_{-0.14}$ dex). We interpret this metallicity spread as strong evidence that the system is a dwarf galaxy as opposed to a star cluster. Combining our velocity measurement with Gaia proper motions, we find that Aquarius III is currently situated near its orbital pericenter in the outer halo ($r_{peri} = 78 \pm 7$ kpc) and that it is plausibly on first infall onto the Milky Way. This orbital history likely precludes significant tidal disruption from the Galactic disk, notably unlike other satellites with comparably low velocity dispersion limits in the literature. Thus, if further velocity measurements confirm that its velocity dispersion is truly below $\sigma_v \lesssim 2\,\mathrm{km\,s^{-1}}$, Aquarius III may serve as a useful laboratory for probing galaxy formation physics in low-mass halos.

Unified Astronomy Thesaurus concepts: Dwarf galaxies (416); Milky Way Galaxy (1054); Local Group (929)

1. Introduction

Cosmological simulations of structure formation within the Lambda cold dark matter (ΛCDM) paradigm strongly suggest that galaxy formation is hierarchical, with massive galaxies and their host dark matter halos forming from the continuous merging and accretion of relatively lower-mass systems (e.g., W. H. Press & P. Schechter 1974; S. D. M. White & M. J. Rees 1978; S. D. M. White & C. S. Frenk 1991). A direct consequence of this bottom-up assembly process is the abundance of substructures around L_* galaxies: galaxies like the Milky Way are expected to be surrounded by scores of accreted subhalos hosting low-mass dwarf galaxies in addition to many orders of magnitude more "dark," very-low-mass subhalos with no luminous counterparts (e.g., B. Moore et al. 1999; V. Springel et al. 2008; B. F. Griffen et al. 2016). The density profiles, mass function, and radial distribution of these subhalos are sensitive probes of the nature of dark matter and its power spectrum on small scales (see J. S. Bullock & M. Boylan-Kolchin 2017, for a review). However, these subhalo properties are challenging to study directly in the absence of a luminous tracer. Thus, the low-mass satellite galaxies inhabiting these small-scale halos have long played a special role as observationally accessible windows into the elusive substructures surrounding the Milky Way and other nearby host galaxies.

At the turn of the 21st century, just 11 satellite galaxies of the Milky Way were known, raising concerns about the consistency of the observed satellite galaxy population with the subhalo population predicted by ΛCDM simulations (G. Kauffmann et al. 1993; A. Klypin et al. 1999; B. Moore et al. 1999). The advent of the Sloan Digital Sky Survey (SDSS) in the early 2000s quickly changed the landscape, however, with the discovery of the first "ultra-faint" stellar systems: exceedingly faint, low-mass satellites beyond the detection limits of prior photographic surveys (e.g., B. Willman et al. 2005a, 2005b; V. Belokurov et al. 2006; D. B. Zucker et al. 2006). Soon after, concerted efforts to spectroscopically characterize the internal velocity and metallicity distributions of these newly discovered systems robustly established their nature as the most dark-matter-dominated, least chemically enriched dwarf galaxies in the universe (J. T. Kleyna et al. 2005; R. R. Muñoz et al. 2006; N. F. Martin et al. 2007; J. D. Simon & M. Geha 2007). In so doing, these studies pointed toward a reconciliation of the completeness-corrected satellite counts with the substructure predicted by ΛCDM (e.g., S. E. Koposov et al. 2009; A. V. Macciò et al. 2010).

Since the early years of SDSS, a succession of sensitive wide-field surveys has continued to drive the rapid discovery of ultra-faint dwarf galaxies in the Galactic halo (e.g., K. Bechtol et al. 2015; A. Drlica-Wagner et al. 2015; D. Kim & H. Jerjen 2015a; S. E. Koposov et al. 2015a, 2018; G. Torrealba et al. 2018; D. Homma et al. 2019, 2023; W. Cerny et al. 2022; M. Gatto et al. 2023; S. E. T. Smith et al. 2023a, 2023b) and throughout the Local Volume (e.g., D. Martínez-Delgado et al. 2022; B. Mutlu-Pakdil et al. 2022; D. J. Sand et al. 2022; M. G. Jones et al. 2023; K. B. W. McQuinn et al. 2023a, 2023b, for recent examples). Paired with advances in numerical simulations (e.g., C. Wheeler et al. 2015; M. Ricotti et al. 2016; F. Munshi et al. 2019; E. Applebaum et al. 2021) and semianalytical modeling (e.g., V. Manwadkar & A. V. Kravtsov 2022; N. Ahvazi et al. 2024; S. Weerasooriya et al. 2023), the large statistical sample of satellites built by these search efforts has not only largely alleviated concerns of tension with ΛCDM (J. S. Bullock & M. Boylan-Kolchin 2017; S. Y. Kim et al. 2018; A. Drlica-Wagner et al. 2020; L. V. Sales et al. 2022) but also enabled wide-ranging and detailed tests of galaxy formation physics and the nature of dark matter (e.g., P. Jethwa et al. 2018; E. O. Nadler et al. 2020, 2021; O. Newton et al. 2021; S. Mau et al. 2022; I. Esteban et al. 2023). Nonetheless, fully leveraging the constraining power of the ultra-faint dwarfs as physical laboratories will require a *complete* census of these systems in the local universe as well as a complete accounting of their dynamical masses and chemistries through follow-up spectroscopy (e.g., J. Simon et al. 2019; E. O. Nadler et al. 2024). Thus, the continued discovery and characterization of these extreme galaxies remains a central focus of "near-field cosmology."

Toward this broader goal, here we present the discovery of DELVE J2348−0329 (Aquarius III), the latest entrant in the ongoing community census of ultra-faint Milky Way satellites with wide-field imaging surveys. In Section 2, we describe our discovery of the satellite and our subsequent deeper follow-up imaging of the system with the 4 m Blanco telescope/DECam. In Section 3, we use this deeper imaging to characterize the satellite's morphology and stellar population. Then, in Section 4, we present Keck II/DEIMOS multiobject spectroscopy of resolved stars in the system from which we measure its intrinsic velocity and metallicity distribution. We then describe our exploration of its brightest stars' chemical abundances based on a Magellan/MagE long-slit spectrum in Section 5. Lastly, we discuss the implications of our measurements for the system's classification, orbital history, and dark matter halo mass in Section 6, and we conclude in Section 7.

Given our eventual determination that DELVE J2348−0329 is an ultra-faint dwarf galaxy as opposed to a star cluster, we follow the historical naming convention for Local Group satellite galaxies and hereafter refer to the system as Aquarius III based on the constellation within which it resides.

2. Discovery and Follow-up Imaging

2.1. Identification in DELVE DR2

The DECam Local Volume Exploration survey (DELVE; A. Drlica-Wagner et al. 2021) is an ongoing campaign to uncover and characterize the satellite populations of the Milky Way, Magellanic Clouds, and several Local Volume hosts with the Dark Energy Camera (DECam; B. Flaugher et al. 2015) on the 4 m Blanco Telescope at Cerro Tololo Inter-American Observatory, Chile. Toward this goal, DELVE has assembled near-contiguous imaging of the southern celestial sky through a combination of 150+ nights of new DECam observations and an extensive reprocessing of archival community observations on the same instrument. The survey's most recent public data release, DELVE DR2 (A. Drlica-Wagner et al. 2022), includes more than 21,000 $\deg^2$ of high-Galactic-latitude sky coverage including $\sim$17,000 $\deg^2$ of overlapping coverage in each of the g, r, i, z bands.

In W. Cerny et al. (2023b), we presented the primary results of our searches for ultra-faint Milky Way satellites over this wide-area data set. These searches relied on the `simple` algorithm,[39] which applies a isochrone matched-filter approach in color–magnitude space (based on the algorithm described in K. Bechtol et al. 2015) to identify overdensities of stars consistent with an old, metal-poor stellar population. From the thousands of candidates identified above our nominal significance threshold of $>5.5\sigma$, we identified a sample of seven especially promising candidates based on both diagnostic plots and on visual inspection of color images from the Legacy Surveys Data Releases 9 and 10 (A. Dey et al. 2019). We presented our discovery and characterization of six of these systems in the aforementioned work but refrained from presenting the seventh candidate—Aquarius III—as the available data were too shallow to robustly confirm its status as a real Milky Way satellite and to characterize its properties. Deeper follow-up imaging has since been obtained and offers clear confirmation of Aquarius III as a bona fide new satellite, as we describe in the subsections below. We note that Aquarius III is the last satellite we anticipate reporting based on searches over DELVE DR2's WIDE component. Ongoing and future searches will focus on the deeper, more homogeneous data set provided by the upcoming DELVE DR3 (see C. Y. Tan et al. 2024 for early results).

2.2. Deeper Imaging with DECam

We obtained dedicated follow-up exposures of Aquarius III with DECam on the nights of 2022 July 28, 31, and 2023 July 14. On each of the former two nights, we collected 3×300 s dithered r-band exposures, while on the latter night we collected 3×300 s g-band exposures and 3×300 s r-band exposures. The majority of these exposures were taken in decent seeing conditions ($\sim$1.″0–1.″3) while Aquarius III was at low air mass ($\sec(z) \lesssim 1.2$); the exception was the first of these nights, when seeing was $\sim$1.″4–1.″5. Owing to the longer integration times compared to the existing data and relatively dark skies, these data typically achieved effective exposure times significantly longer than the previously available data from public DECam surveys.

We processed these 12 new exposures, as well as all existing archival g, r-band exposures of the same field, using a pipeline similar to that used for the Dark Energy Survey (DES) Year 3 cosmology analyses (W. G. Hartley et al. 2021; I. Sevilla-Noarbe et al. 2021). This processing is described in more detail by C. Y. Tan et al. (2024) in the context of early science results from DELVE Data Release 3; however, we highlight here that this pipeline relies on image-level coaddition for detection, followed by simultaneous fits to all individual images, to derive the full benefit from overlapping exposures of the same area. This is in contrast to the processing used for DELVE DR1 and DELVE DR2, which constructed multiband catalogs by collating measurements made on individual exposures (as originally introduced by A. Drlica-Wagner et al. 2015). The combined effect of the new exposures and the coadd image processing improved the 10σ depth of our catalogs to g_0, $r_0 \sim 24.5$, representing a nearly 1 magnitude improvement in each band relative to the median depth of DELVE DR2 despite the relatively modest investment of additional exposure time.

For all analyses described below, we used a cleaned version of this catalog that retained only sources that passed the SourceExtractor cuts `FLAGS` < 4 and `IMAFLAGS_ISO` $= 0$ in each band (see, e.g., T. M. C. Abbott et al. 2021 for a description of these parameters).[40] We specifically made use of the "Single Object Fitting" point-spread function magnitudes derived from the coadd processing, which we corrected for interstellar extinction using the maps of D. J. Schlegel et al. (1998) with the recalibration from E. F. Schlafly & D. P. Finkbeiner (2011). Stars were separated from background galaxies using a morphological classifier (`EXTENDED_CLASS`) based on the distribution of sources in the `BDF_T`–`BDF_S2N` plane, where `BDF_T` is a parameter describing the best-fit preseeing bulge + disk model size (W. G. Hartley et al. 2021), and `BDF_S2N` is the associated signal-to-noise. This classifier, which was developed for DES Y6, assigns sources an integer score from 0 to 4, with 0 being the most point-like. For our analysis, we adopted a selection $0 <=$ EXTENDED_CLASS_G $<= 2$ based on measurements derived from the g-band images but note that using different thresholds did not significantly influence our results.

2.2.1. A Clearer Look at Aquarius III

In Figure 1, we present several views of Aquarius III based on the deeper DECam photometric catalog described above. In the leftmost panels, we depict the spatial distribution of stars and galaxies in a small region around the candidate system after filtering with an old, metal-poor isochrone and smoothing the resulting density field with a Gaussian kernel. Comparing the density of stars within a 5′ radius to that measured from an equal-area concentric background annulus with an inner radius $r = 12'$ away, Aquarius III stands out as a robust overdensity of stars with a Poisson significance of $\sim 7\sigma$. The detection of this as-yet unreported stellar system is further elucidated by its color–magnitude diagram (CMD; center-left panel), which clearly displays a distinct lower red giant branch (RGB), main-sequence turnoff (MSTO), and upper main-sequence (MS) characteristic of an old, metal-poor halo stellar population. These features are not seen for the sample of stars in a concentric control annulus (center right panel), as emphasized by a background-subtracted Hess diagram (far-right-hand panel). The MSTO feature that clearly appears in these panels

[39] https://github.com/DarkEnergySurvey/simple

[40] We make this deeper catalog available in an online repository associated with this work (see Data Availability section).

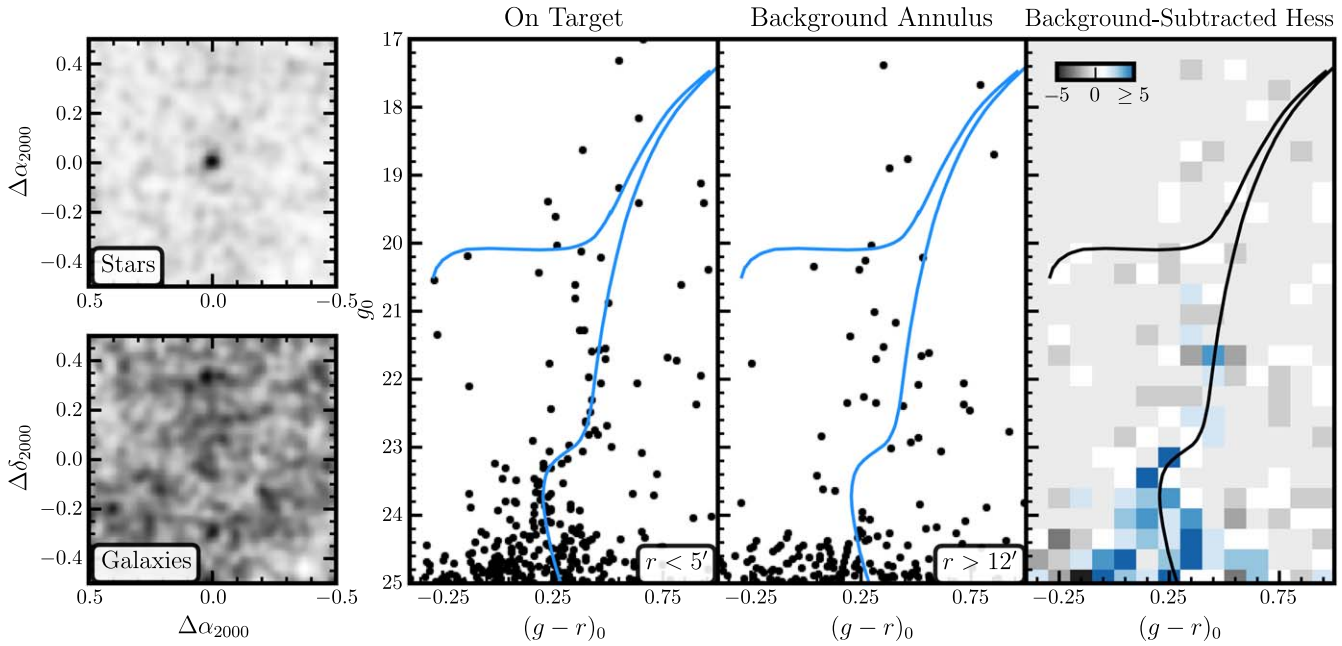

Figure 1. Diagnostic views of Aquarius III based on the deeper DECam photometric catalog described in Section 2.2. Far left: isochrone-filtered spatial distribution of stars (top subpanel) and galaxies (bottom subpanel) in a 1.0° × 1.0° region centered on Aquarius III. In both of these panels, a magnitude cut of $g_0 < 25$ has been applied, and the (normalized) filtered density field has been smoothed with a Gaussian kernel. Center panels: color–magnitude diagrams of stars within a $r = 5'$ region (center left) and in concentric, equal-area background annulus with inner radius $r = 12'$ (center right). An old, metal-poor stellar isochrone with $\tau = 13.5$ Gyr, $Z = 0.0001$ is shown as a solid blue curve. Far right: Hess diagram constructed by subtracting the binned background CMD from the binned on-target CMD. This diagram clearly reveals the lower RGB, subgiant branch, and MSTO of Aquarius III while also making the paucity of brighter upper RGB stars apparent.

was only marginally visible in the discovery CMD from DELVE DR2, emphasizing the importance of the deeper follow-up imaging for characterization of the putative stellar system.

3. Structural and Stellar Population Properties

We simultaneously fit Aquarius III's structure and stellar population with the Ultra-faint Galaxy LIkelihood (`ugali`) toolkit,[41] which implements the unbinned Poisson maximum-likelihood formalism described in Appendix C of A. Drlica-Wagner et al. (2020). Aquarius III was modeled with an H. C. Plummer (1911) radial stellar density profile, and its g-, r-band CMD was fit with a PARSEC stellar isochrone (A. Bressan et al. 2012; Y. Chen et al. 2014, 2015, Version 1.2S). The main free parameters of the radial profile model were Aquarius III's centroid coordinates (α_{2000} and δ_{2000}), angular elliptical half-light radius (a_h), ellipticity (ϵ, defined as $\epsilon = 1 - \frac{b}{a}$), and position angle (P.A.) east of north. The isochrone age was fixed at $\tau = 13.5$ Gyr, and the metallicity was fixed at $Z = 0.0001$ (the oldest age and lowest metallicity in our grid), and thus the only free parameter for the CMD component of the fit was the distance modulus, $(m - M)_0$. Lastly, as an additional free parameter, `ugali` models the "richness" of the putative satellite, which is defined as the total number of stars in the system above the hydrogen-burning limit (A. Drlica-Wagner et al. 2020).

We derived posterior probability distributions for each of the seven free model parameters using the affine-invariant Monte Carlo Markov Chain (MCMC) sampler `emcee` (D. Foreman-Mackey et al. 2013), for which we used 80 walkers each taking 15,000 steps with the first 3000 steps discarded as burn-in. In Table 1, we report the resulting estimates of the model parameters and their uncertainties where the uncertainties were derived in most cases from the highest density interval containing the peak and 68% of the marginalized posterior distribution. We also report a number of additional quantities derived from these posteriors, including Aquarius III's azimuthally averaged angular and physical half-light radii (r_h and $r_{1/2}$, respectively, where $r_h = a_h\sqrt{1-\epsilon}$), absolute magnitude ($M_V$, derived using the formalism from N. F. Martin et al. 2008), V-band luminosity ($L_V \equiv 10^{0.4(4.83-M_V)}$), and stellar mass ($M_*$, calculated from L_V assuming a stellar-mass-to-light ratio of 2).

All of these results were specifically derived from a fit using our deeper DECam catalog with an assumed magnitude limit of g_0, $r_0 = 24.25$ and both the isochrone age and metallicity fixed. We estimate the formal S/N = 10 mag limit of our deeper DECam catalog to be g_0, $r_0 \approx 24.5$, but chose to use a more conservative limit for our analysis to derive measurements in a regime where the star/galaxy classification and photometric uncertainties are better controlled.

3.1. Summary of Structural Fit Results

We find that Aquarius III is a low-luminosity ($M_V = -2.5^{+0.3}_{-0.5}$, $L_V = 850^{+380}_{-260}\ L_\odot$) Milky Way satellite with a CMD that is fit closely by the oldest, most metal-poor isochrone in our PARSEC grid. The satellite's structure is well fit by an H. C. Plummer (1911) radial stellar density profile with an elliptical half-light radius $a_h = 2.1^{+0.7}_{-0.5}{}'$ ($a_{1/2} = 51^{+16}_{-12}$ pc) and a moderate ellipticity ($\epsilon = 0.47^{+0.14}_{-0.28}$). The corresponding azimuthally averaged half-radius is $r_h = 1.6^{+0.4}_{-0.3}{}'$ ($r_{1/2} = 41^{+9}_{-8}$ pc). The total number of observed (photometric) members above our nominal magnitude limit, calculated by summing over the

[41] https://github.com/DarkEnergySurvey/ugali

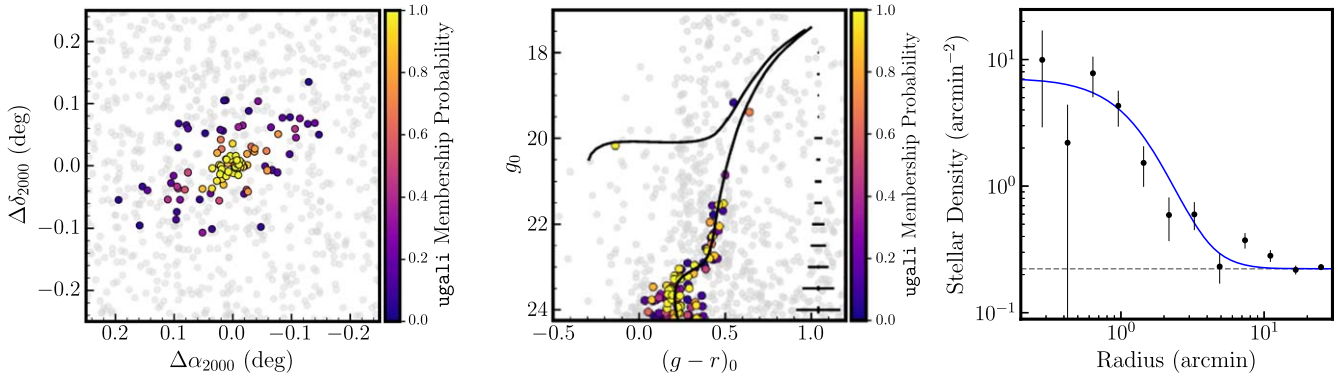

Figure 2. Left: spatial distribution of stars in a $0.5° \times 0.5°$ region centered on Aquarius III. All stars are colored by their membership probabilities assigned by our `ugali` fit, which incorporates both spatial and color–magnitude information but does not include velocity or metallicity information from our spectroscopy. Stars with probabilities $p < 0.05$ are shown in gray for ease of visualization. Center: CMD for sources in the left-hand panel, with the same coloring scheme. A PARSEC isochrone with age 13.5 Gyr and metallicity $Z = 0.0001$, shifted to a distance modulus $(m - M)_0 = 19.66$, is shown as a solid black curve. Right: radial stellar density profile of isochrone-filtered stars derived from concentric circular bins (black points, with Poisson uncertainties shown) assuming the same magnitude cuts and star/galaxy separation criterion as used for the `ugali` fit. The best-fitting Plummer model with azimuthally averaged angular half-light radius $r_h = 1.'6$ is shown in blue.

Table 1
Properties of the Aquarius III Milky Way Satellite Galaxy

Parameter	Description	Value	Unit	Section
α_{2000}	Centroid right ascension	$357.218^{+0.005}_{-0.004}$	deg	3
δ_{2000}	Centroid declination	$-3.489^{+0.004}_{-0.003}$	deg	3
a_h	Elliptical angular half-light radius	$2.1^{+0.7}_{-0.5}$	arcmin	3
$a_{1/2}$	Elliptical physical half-light radius	51^{+16}_{-12}	pc	3
r_h	Azimuthally averaged angular half-light radius	$1.6^{+0.4}_{-0.3}$	arcmin	3
$r_{1/2}$	Azimuthally averaged physical half-light radius	41^{+9}_{-8}	pc	3
ϵ	Ellipticity	$0.47^{+0.14}_{-0.28}$	...	3
P.A.	Position angle of major axis (east of north)	119^{+17}_{-11}	deg	3
$(m - M)_0$	Distance modulus	19.66 ± 0.11[a]	mag	3
$D_\odot$	Heliocentric distance	85 ± 4[a]	kpc	3
M_V	Absolute V-band magnitude	$-2.5^{+0.3}_{-0.5}$	mag	3
L_V	V-band luminosity	850^{+380}_{-260}	$L_\odot$	3
M_*	Stellar mass (assuming $M_*/L_V = 2$)	1700^{+760}_{-520}	$M_\odot$	3
$E(B - V)$	Mean reddening ($r < 5'$)	0.04	mag	3
$N_{\rm spec}$	Number of spectroscopic members	11	...	4.4
$v_{\rm sys}$	Mean heliocentric radial velocity	$-13.1^{+1.0}_{-0.9}$	km s^{-1}	4
σ_v	Velocity dispersion,[b] uniform prior $0 < \sigma_v < 10$	<3.5	km s^{-1}	4.5
σ_v	Velocity dispersion, prior: $\lvert\log_{10}\sigma_v\rvert < 1$	<2.1	km s^{-1}	4.5
$M_{1/2}$	Dynamical mass within $r_{1/2}$	$<5.1 \times 10^5$	$M_\odot$	4.6
$M_{1/2}/L_{V,1/2}$	Mass-to-light ratio within $r_{1/2}$	<1300	$M_\odot/L_\odot$	4.6
$\log_{10} J(0.^\circ 5)$	J-factor within a solid angle of radius 0.5°	<17.8	GeV^2 cm^{-5}	6.4
$[{\rm Fe/H}]_{\rm spec}$	Mean spectroscopic metallicity	-2.61 ± 0.21	dex	4.7
$\sigma_{\rm [Fe/H]}$	Metallicity dispersion among spectroscopic members	$0.46^{+0.26}_{-0.14}$	dex	4.7
$\mu_{\alpha*}$	Proper motion in right ascension	1.01 ± 0.25	mas yr^{-1}	6.2
μ_δ	Proper motion in declination	-0.10 ± 0.20	mas yr^{-1}	6.2
$r_{\rm GC}$	Galactocentric distance	86 ± 4	kpc	6.2
$r_{\rm apo}$	Orbital apocenter	Unconstrained	kpc	6.2
$r_{\rm peri}$	Orbital pericenter	78 ± 7	kpc	6.2
e	Orbital eccentricity	Unconstrained	...	6.2
L_Z	Angular momentum about the galactocentric Z-axis	13^{+3}_{-5}	10^3 kpc km s^{-1}	6.2

Notes. The velocity dispersion posterior peaked near zero, and we therefore quote upper limits for σ_v, $M_{1/2}$, $M_{1/2}/L_{V,1/2}$, and $\log_{10} J(0.^\circ 5)$ at the 95% credible level.
[a] We assume a ± 0.1 mag systematic uncertainty on the distance modulus to account for uncertainties in isochrone modeling following A. Drlica-Wagner et al. (2015). This systematic term has been propagated to the quoted heliocentric distance in kiloparsecs as well as to our physical size measurements.
[b] We recommend the use of this velocity dispersion limit derived assuming the uniform prior on $0 < \sigma_v/({\rm km\ s^{-1}}) < 10$. We use this estimate when deriving the dynamical mass and mass-to-light ratio reported in the subsequent rows.

membership probabilities computed by ugali, is $\Sigma p_{i,\mathrm{obs}} \sim 56$ stars.

We visualize all of these results in Figure 2, where we show the spatial distribution and CMD of stars in the system in the left and center panels, respectively, as well as its radial profile in the right-hand panel. Stars in the former two panels are colored by their membership probabilities from our ugali fit, which incorporates both spatial and color–magnitude information but no spectroscopic information.

4. Stellar Kinematics and Metallicities from Keck/DEIMOS Spectroscopy

4.1. Observations and Data Reduction

To characterize Aquarius III's mean velocity, internal kinematics, and stellar metallicities, we obtained medium-resolution, multiobject spectroscopy of stars in Aquarius III with the DEep Imaging Multi Object Spectrograph (DEIMOS; S. M. Faber et al. 2003) on the Keck II telescope at the W.M. Keck Observatory on Maunakea, Hawai'i. Following numerous past studies of Milky Way satellites with DEIMOS (e.g., N. F. Martin et al. 2007; J. D. Simon & M. Geha 2007), we used the 1200 G grating with the OG550 order-blocking filter. This configuration provides near-continuous coverage over the wavelength range 6500–9000 Å at a resolution of $\mathcal{R} \sim 6500$. This wavelength range contains a number of strong stellar absorption features including Hα, the calcium triplet (CaT), and the Mg I λ8807 line, in addition to the strong telluric *A*-band feature at ∼7600 Å.

On the night of 2023 October 5, we collected 1×1200 s, 7×1800 s, and 1×1500 s exposures for a total shutter-open exposure time of 15,300 s (4.25 hr), all in clear conditions.[42] We used a single multiobject mask comprised of slits of width 0.″7 and minimum length 4.″5. Targets for this mask were drawn primarily from the probabilistic member catalog provided by a preliminary ugali fit (see Section 3) as well as from an additional pool of targets drawn from the DESI Legacy Imaging Surveys Data Release 10 (A. Dey et al. 2019). XeNeArKr arcs and internal quartz flats were taken at the beginning of the night; this is sufficient for precise wavelength calibration thanks to DEIMOS' excellent stability and active flexure compensation system.

The raw DEIMOS spectra were reduced using a lightly modified version of the official Keck-supported data reduction pipeline implemented within the PypeIt framework (J. Prochaska et al. 2020). PypeIt reduces the eight DEIMOS CCDs as four separate mosaic images each containing a red and blue chip and automatically performs flat-fielding, sky subtraction, and spectral extraction followed by wavelength calibration based on the calibration arc frames. For the reductions used here, we disabled PypeIt's default flexure corrections and heliocentric velocity corrections, and we instead determined linear flexure corrections for each reduced 1D spectrum during our velocity measurement procedure described below.

4.2. Velocity Measurements

We measured line-of-sight velocities of stars using an in-development version of the DMOST package (M. Geha et al. 2024, in preparation),[43] a dedicated measurement pipeline for observations made with DEIMOS' 1200G grating. DMOST measures stellar velocities by forward-modeling the 1D spectrum of a given star with both a stellar template from the PHOENIX stellar atmosphere library (T. O. Husser et al. 2013) and a telluric absorption spectrum from TelFit (K. Gullikson et al. 2014). The stellar spectrum template is selected from a coadded spectrum derived from all exposures of a given source, while the telluric template is selected based on a fit to the highest signal-to-noise ratio (S/N) sources on a given mask (for each exposure) and is assumed to be representative across all sources on the mask. After these templates have been selected, velocities are determined on an exposure-by-exposure basis by minimizing the χ^2 of the best-fit template against the observed spectrum from each exposure. This is carried out through an MCMC fit simultaneously constraining both the radial velocity of a given star as well as a linear wavelength shift of the telluric spectrum needed to correct for the miscentering of stars within their slits (see S. T. Sohn et al. 2007). If no individual exposures yielded a velocity measurement (as commonly occurs for the very faintest sources), DMOST instead derives the velocity from the coadded spectrum across all exposures.

The final radial velocity of a given star is calculated from an inverse-variance-weighted average across the measurements from individual exposures that had well-behaved (nearly Gaussian) posteriors. The associated statistical error is taken as the standard deviation across exposures. Lastly, a total velocity error that includes the contribution of systematic effects was calculated by scaling this statistical error by a factor of 1.4 and adding an additional 1.1 km s^{-1} in quadrature, i.e., $\epsilon^2_{v,\mathrm{tot}} = \sqrt{1.4\epsilon^2_{\mathrm{v,stat}} + 1.1^2}$. Here, the scaling term encapsulates the S/N-dependent component of the systematic error while the fixed term represents an uncertainty floor. This systematic error prescription was derived based on the repeatability of velocity measurements across hundreds of DEIMOS masks. The total uncertainties from this procedure have been validated by comparing stellar velocities against public radial velocity data from large-scale spectroscopic surveys (M. Geha et al. 2024, in preparation).[44]

4.3. Equivalent Width Measurements

DMOST also measures the equivalent widths (EWs) of the CaT lines of stellar sources from their coadded 1D spectra. For this work, each of the CaT lines was modeled with a Gaussian-plus-Lorentzian profile (for stars at S/N > 15 per spectral pixel) or a Gaussian profile (for stars at S/N < 15 pixel^{-1}). The profile model parameters were derived through a nonlinear least-squares fit using scipy (P. Virtanen et al. 2020), and we integrated the resulting fits to get the EW of each line. The statistical error on the EW of each line was then derived analytically from the fit errors. Lastly, a total CaT EW error was computed by summing the EW uncertainties of the three individual lines in quadrature and then further adding a 0.2 Å systematic uncertainty floor in quadrature. Analogously to the velocity uncertainties, this systematic uncertainty floor was derived based on the repeatability of total EW measurements

[42] The mean Modified Julian Day (MJD) of these exposures was 60223.40527.
[43] https://github.com/marlageha/dmost
[44] We emphasize that this systematic error prescription is not just instrument dependent: it is *pipeline dependent*. Thus, this prescription is not generally applicable to all DEIMOS analyses nor is it expected to match other prescriptions in the literature.

Table 2
Basic Properties of Stars Observed with Keck/DEIMOS

Star Name	R.A.	Decl.	g_0	r_0	S/N	$v_{\rm hel.}$	Σ EW CaT	[Fe/H]	Member	Type
Gaia DR3 2447566690779941504	357.216	−3.488	19.41	18.77	78.1	−14.5 ± 1.2	1.80 ± 0.21	−3.05 ± 0.11	True	RGB
Gaia DR3 2447566656420203008	357.239	−3.489	20.19	20.33	25.7	−11.1 ± 1.9	⋯	⋯	True	BHB
Aqu III J234851.34−032925.89	357.214	−3.491	21.56	21.10	17.0	−12.9 ± 2.2	3.03 ± 0.28	−1.95 ± 0.13	True	RGB
Aqu III J234849.41−032917.06	357.206	−3.488	21.53	21.04	15.5	−12.5 ± 2.0	1.52 ± 0.29	−2.81 ± 0.15	True	RGB
Aqu III J234851.13−032916.12	357.213	−3.488	21.71[a]	21.27[a]	12.6	−13.6 ± 3.2	1.56 ± 0.30	−2.74 ± 0.15	True	RGB
Aqu III J234848.22−032927.00	357.201	−3.491	22.06	21.60	9.4	−10.9 ± 4.9	2.09 ± 0.34	−2.34 ± 0.17	True	RGB
Aqu III J234855.22−032840.90	357.230	−3.478	22.30	21.87	7.2	−10.3 ± 5.5	1.41 ± 0.37	−2.74 ± 0.19	True	RGB
Aqu III J234838.64−032753.36	357.161	−3.465	22.47	22.05	6.5	−19.9 ± 5.6	2.23 ± 0.48	−2.17 ± 0.22	True	RGB
Aqu III J234850.46−032929.86	357.210	−3.492	22.64	22.24	5.3	−17.8 ± 5.9	2.52 ± 0.58	−1.97 ± 0.28	True	RGB
Aqu III J234846.51−032915.26	357.194	−3.488	22.75	22.31	5.0	−7.1 ± 6.9	1.96 ± 0.51	−2.27 ± 0.25	True	RGB
Aqu III J234901.54−033156.18	357.256	−3.532	22.81	22.36	4.2	−5.4 ± 8.0	1.78 ± 0.56	−2.39 ± 0.27	True	RGB
Aqu III J234856.79−033032.90	357.237	−3.509	22.60	22.21	19.0	−11.2 ± 1.5	5.66 ± 0.27	⋯	False	⋯
Gaia DR3 2447566690779941120	357.225	−3.491	20.79	19.47	13.1	−11.5 ± 1.6	3.69 ± 0.32	⋯	False	⋯
Gaia DR3 2447567137456807936	357.123	−3.497	20.10	19.12	67.6	−30.8 ± 1.1	4.85 ± 0.31	⋯	False	⋯
Gaia DR3 2447566656420202624	357.248	−3.491	20.42	20.24	28.1	−250.8 ± 1.8	⋯	⋯	False	BHB
Aqu III J234910.87−033040.95	357.295	−3.511	21.28	20.91	14.1	−207.9 ± 2.3	3.21 ± 0.31	⋯	False	⋯
Aqu III J234832.38−032729.57	357.135	−3.458	22.94	21.97	12.5	−117.0 ± 1.2	1.00 ± 1.48	⋯	False	⋯
Aqu III J234846.59−032810.30	357.194	−3.470	21.96	21.55	9.6	−125.9 ± 3.3	3.38 ± 0.40	⋯	False	⋯
Aqu III J234817.17−032618.61	357.072	−3.439	22.34	21.92	5.7	−138.3 ± 5.7	3.97 ± 0.61	⋯	False	⋯

Notes. Stars are separated by membership category with the confirmed members first, followed by the two velocity-consistent nonmembers, and lastly, the six nonmembers. Celestial coordinate positions (R.A., decl.) and extinction-corrected magnitudes are taken from our deeper DECam photometric catalog. The quoted signal-to-noise ratio (S/N) reported here relate to the DEIMOS spectroscopy. Note that metallicities derived from spectra below S/N = 7 may be less reliable and thus were excluded from our metallicity dispersion fit.

[a] This star was found to have inconsistent *r*-band photometry between our deeper DECam catalog and Legacy Surveys DR10, such that it would have been rejected in the former data set by a CMD selection. Given the star's spectrum, velocity, central position, and lack of obvious time variability, we choose to adopt the LS DR10 *r*-band magnitude and therefore consider this star is indeed a true member.

across masks and validated against spectroscopic metallicities from large-scale public surveys.

From these CaT EW measurements, we derived [Fe/H] measurements for all candidate RGB stars assuming the luminosity-dependent EW–[Fe/H] calibration from R. Carrera et al. (2013). We specifically adopted the form of the calibration that requires the absolute *V*-band magnitude of each source as an input, which we estimated by transforming our DECam *g*, *r* photometry using the piecewise relations derived for DES DR2 (Appendix B of T. M. C. Abbott et al. 2021) and subtracting our derived distance modulus of $(m-M)_0 = 19.66 \pm 0.11$. Posterior distributions for the metallicity of a given star were constructed through Monte Carlo sampling from the error distributions on the total EWs (including the assumed 0.2 Å systematic error), the *g*, *r*-band photometry,[45] Aquarius III's distance modulus, and the coefficients on the R. Carrera et al. (2013) relation; we assumed Gaussian errors in all cases. Our final metallicity measurements were then derived based on the median and 16th/84th percentiles of the resultant posteriors.

Lastly, we also used `DMOST` to measure the EW of the Mg I λ8807 absorption line. The strength of this line is correlated with stellar surface gravity, and thus, its EW is a useful discriminant for separating foreground MS stars from red giants such as those expected in a halo dwarf galaxy (G. Battaglia & E. Starkenburg 2012). We performed a simple Gaussian fit to this line through a procedure like that used for the CaT and integrated to get the EW. The errors on the Mg I EW measurements have not been extensively validated, and here, we opted to only use these measurements to retroactively check that our member sample did not include any interloper MS stars with large Mg I EWs.

[45] We add a 0.02 mag uncertainty floor in quadrature to the photometric errors in each filter to account for zero-point uncertainties.

4.4. Stellar Membership

The measurement procedures described above yielded a sample of 19 stars with reliable velocity measurements. We report the basic properties for these 19 stars in Table 2, including their positions, apparent magnitudes, velocities, metallicities, and the S/N of their coadded DEIMOS spectra. At a glance, the S/Ns of stars in our sample range from $S/N = 78\ \mathrm{pixel}^{-1}$ for the brightest star ($g_0 \sim 19.4$) down to $S/N = 4\ \mathrm{pixel}^{-1}$ for the faintest ($g_0 \sim 22.8$). The full range of velocity errors is 1.2–8.0 km s^{-1}, with measurements at $S/N \gtrsim 15\ \mathrm{pixel}^{-1}$ generally being dominated by the systematic uncertainty component. The CaT EW uncertainties span ∼0.2–0.6 Å; however, we opted to exclude EW measurements derived from spectra at $S/N < 7\ \mathrm{pixel}^{-1}$ from our analysis. In practice, this means we considered only stars with CaT EW measurements uncertainties less than 0.4 Å.

In Figure 3, we visualize the properties of all 19 stars in a CMD (left panel), the $v_{\rm hel}$–CaT EW plane (center panel), and in a proper-motion vector-point diagram (right panel) derived using measurements available from Gaia Data Release 3 (Gaia Collaboration et al. 2023). As seen in the center panel, the velocity distribution of this 19-star sample includes a conspicuous excess of 13 stars in the velocity range $-20\ \mathrm{km\ s^{-1}} \lesssim v_{\rm hel.} \lesssim 0\ \mathrm{km\ s^{-1}}$. Of these 13 stars, 12 are consistent with the best-fit isochrone from our `ugali` fit. The remaining star, Gaia DR3 2447566690779941120, is ∼0.8 mag redder than the best-fit isochrone, and we therefore

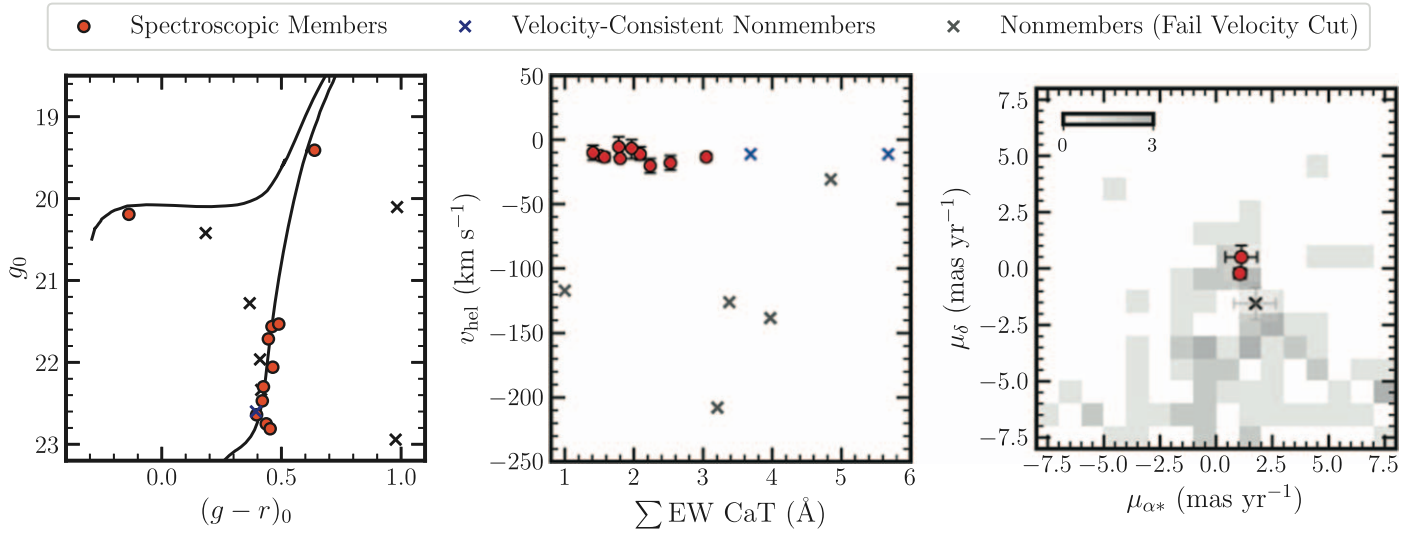

Figure 3. Three views of our Keck/DEIMOS spectroscopic sample for the Aquarius III field. In each panel, our sample of confirmed members are shown as red filled circles while nonmembers are shown as blue and black crosses. Left: CMD showing just the spectroscopic sample. One velocity-consistent nonmember is redder and falls outside the axis limits shown here. Center: radial velocity in the heliocentric frame ($v_{\rm hel.}$) vs. summed equivalent width of the calcium triplet lines (Σ EW CaT). No CaT EW error bars are shown for ease of visualization. The suspected members of Aquarius III cluster in the velocity range $-20 < v_{\rm hel.}/({\rm km\ s^{-1}}) < 0$, and all share low CaT EWs. Note that the BHB star has been excluded from this central panel as its CaT EW is not well measured due to the strong Paschen absorption in its spectrum. Right: Gaia proper motions of the spectroscopic sample overlaid over a 2D histogram of the proper motions of all stars within a 10′ radius. Only the brightest two spectroscopic members have reported proper motions from Gaia. These two members' proper motions are closely consistent with each other and form the basis of our measurement for the Aquarius III system.

rejected it from membership despite its consistent velocity. We then further rejected one of the 12 velocity-consistent, isochrone-consistent stars (J234856.79−033032.90) because its implied metallicity, $[{\rm Fe/H}] = -0.44 \pm 0.14$, would be inconsistent with the remaining member candidates and the composite metallicity distribution of known ultra-faint dwarf galaxy stars (see, e.g., Figure 11 of S. W. Fu et al. 2023). This star also exhibited a noticeably higher Mg I EW than the remaining member candidates, 0.48 ± 0.17 Å (statistical error only), further suggesting its nature as a foreground MS contaminant.

After these selections, we were left with a sample of 11 stars, which we regard as clear members of Aquarius III including 10 RGB stars and one blue horizontal branch (BHB) star. Within the sample of 10 plausible RGB member stars with similar velocities, all were found to have a Mg I EW measurement consistent with being giants according to the G. Battaglia & E. Starkenburg (2012) criterion at the $<1.5\sigma$ level. In addition, the candidate BHB star displays the broad Paschen absorption lines expected from a BHB star of its temperature. Thus, we found no reason to exclude any stars, and we regard all 11 of these velocity-selected stars as likely members of Aquarius III.

4.5. Velocity and Velocity Dispersion

We derived estimates of Aquarius III's systemic radial velocity ($v_{\rm sys}$) and velocity dispersion (σ_v) through a simple two-parameter fit assuming the likelihood from M. G. Walker et al. (2006). The observed velocity distribution was modeled as a Gaussian distribution with mean $v_{\rm sys}$ and a dispersion constituted both by an intrinsic component σ_v and a component associated with the observational errors. We then performed a Bayesian fit assuming a default uniform prior on the velocity dispersion of $0 < \sigma_v/({\rm km\ s^{-1}}) < 10$. Posterior probability distributions for each parameter were derived through MCMC sampling with `emcee`; for this sampling, we used 100 walkers each taking 6000 steps with the first 1000 steps for each walker discarded as burn-in. The resulting posteriors are shown in the left side of Figure 4.

From the median and 16th/84th percentile of the marginalized posterior distribution, we found a systemic velocity of $v_{\rm sys} = -13.1^{+1.0}_{-0.9}$ km s^{-1} for Aquarius III. For the velocity dispersion, σ_v, the MCMC sampling produced marginalized posterior distributions with a mode approaching the lower boundary of our velocity dispersion prior ($\sigma_v = 0$). We are therefore only able to place an upper limit on the dispersion, which we find to be $\sigma_v < 3.5$ km s^{-1} (95% credible upper limit) for our default prior. This limit strengthens to $\sigma_v < 2.1$ km s^{-1} at the 95% credible level if we instead adopt a log-uniform prior of $-1 < \log_{10}(\sigma_v) < 1$.[46] We adopt the first of these as our nominal measurement because it most accurately reflects our prior belief on the range of possibility velocity dispersions of the system. Moreover, we view this as the most conservative choice for the sake of interpreting Aquarius III's seemingly low mass (see Section 6.3).

4.6. Dynamical Mass and Mass-to-light Ratio

We proceeded to place an upper limit on Aquarius III's dynamical mass within the half-light radius ($M_{1/2}$) using the mass estimator from J. Wolf et al. (2010):

$$M_{1/2} = 930\ M_\odot \left(\frac{\sigma_v}{\rm km\ s^{-1}}\right)^2 \left(\frac{r_{1/2}}{\rm pc}\right),$$

under the assumption that the system is in dynamical equilibrium. We constructed the posterior distribution of $M_{1/2}$ by directly Monte Carlo sampling from the posterior distributions for $r_{1/2}$ and σ_v without replacement and transforming them according to this relation. This yielded an upper limit on

[46] For the logarithmic prior, the MCMC sampling was performed over $\log_{10}(\sigma)$. We then recasted the samples to linear σ_v estimates in order to quote upper limits.

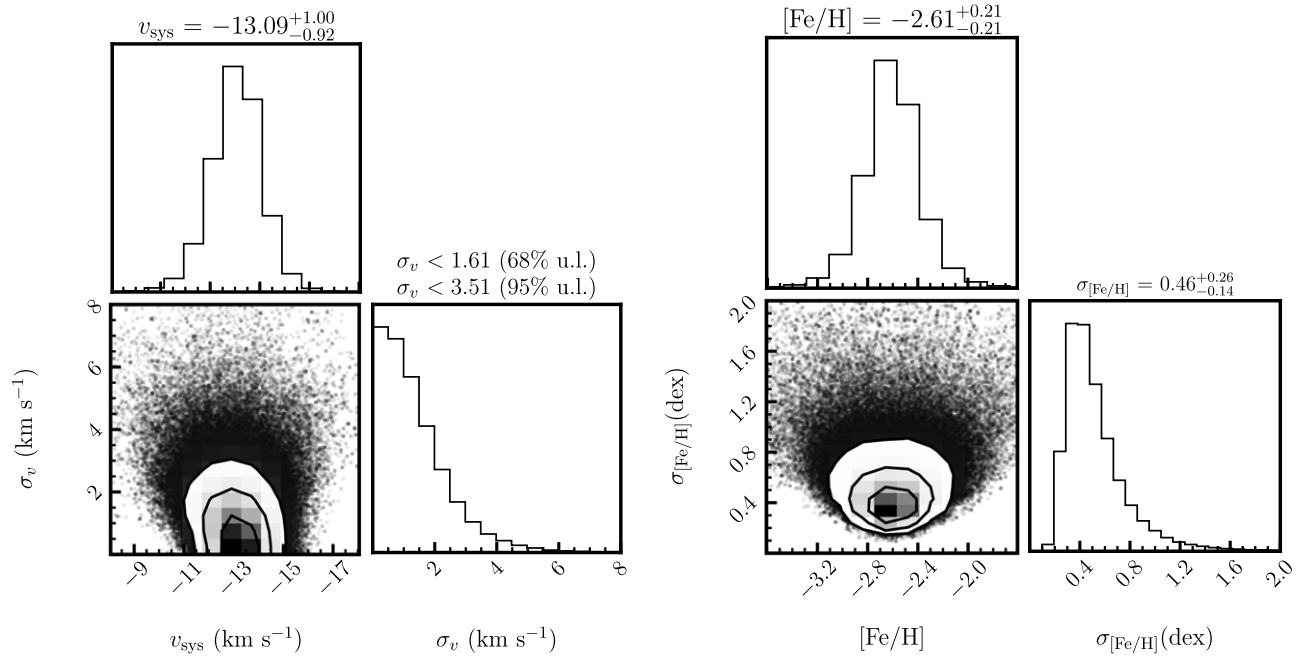

Figure 4. Left: posterior distributions for Aquarius III's systemic mean velocity ($v_{\rm sys}$) and velocity dispersion (σ_v), derived from all 11 member stars assuming a uniform prior of $0 < \sigma_v/({\rm km\ s^{-1}}) < 10$. The velocity dispersion is unresolved with an upper limit of 3.5 km s^{-1} at the 95% credible level. Right: the equivalent posterior distributions for Aquarius III's systemic metallicity ([Fe/H]) and metallicity dispersion ($\sigma_{\rm [Fe/H]}$), derived from the six RGB member stars. The metallicity dispersion is clearly nonzero with a 95% (99.5%) credible lower limit of 0.25 (0.19) dex.

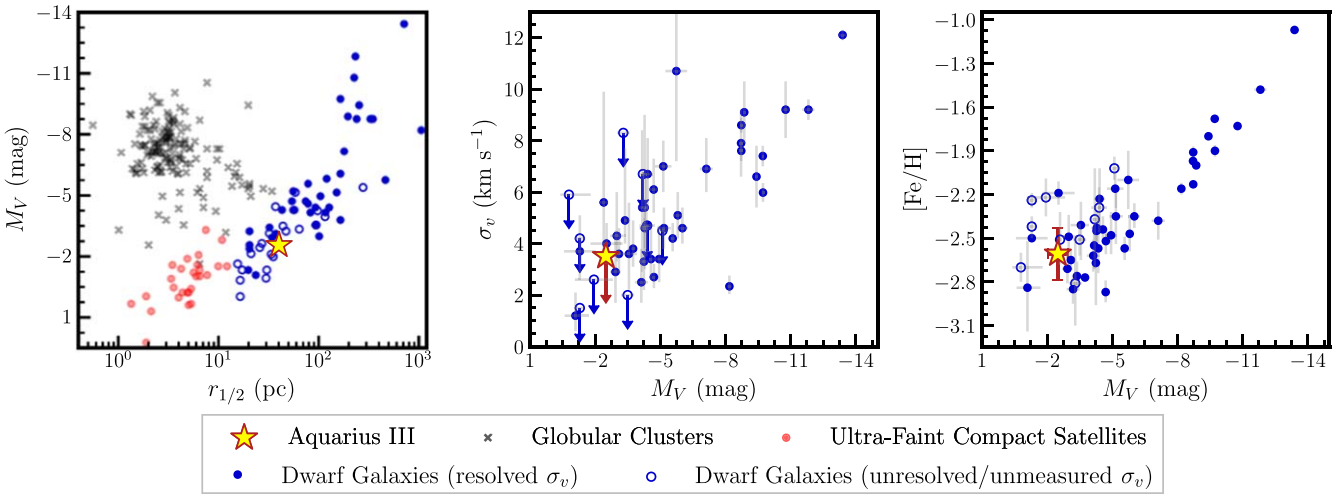

Figure 5. Left: absolute magnitude vs. half-light radius for the known population of Milky Way satellite galaxies (excluding the LMC, SMC, and Sagittarius), "classical" globular clusters, and ultra-faint, compact systems generally presumed to be star clusters. Center: velocity dispersion vs. absolute magnitude for the population of known Milky Way satellite galaxies for which spectroscopic measurements are available (blue circles; excluding the LMC, SMC, and Sagittarius) and for Aquarius III (yellow star). Upper limits are denoted by downward arrows. Aquarius III's velocity dispersion upper limit is comparable to the upper limits observed for other faint satellite galaxies. Right: spectroscopic metallicity vs. absolute magnitude for the same population of satellite galaxies. Aquarius III falls comfortably near the M_V–[Fe/H] sequence delineated by the population of known Milky Way satellites. A complete reference list for the underlying measurements is provided in the Appendix.

Aquarius III's dynamical mass within the half-light radius of $M_{1/2} < 5.1 \times 10^5\, M_\odot$ at the 95% credible level. Adopting a luminosity within the half-light radius of $L_{1/2} \equiv 0.5 L_V = 425^{+190}_{-130}\, L_\odot$, this dynamical mass implies an upper-limit on the mass-to-light ratio within $r_{1/2}$ of $M_{1/2}/L_{1/2} < 1300\, M_\odot/L_\odot$ (at the 95% credible level).

Taken at face value, this mass-to-light ratio limit suggests that Aquarius III is consistent with having a substantial amount of dark matter or none at all. We therefore conclude that the available kinematic data do not clearly distinguish whether the system is a dark-matter-dominated dwarf galaxy or a baryon-dominated, self-gravitating star cluster. This being said, we are able to eventually conclude that Aquarius III is a dark-matter-dominated dwarf galaxy based on its size and metallicity distribution (see Figure 5 and Section 6.1). In this light, our relatively strong limits on Aquarius III's velocity dispersion and total mass may position the galaxy as a useful laboratory for studying galaxy formation in low-mass halos (see Section 6.3).

4.7. Metallicity and Metallicity Dispersion

We also derived estimates of Aquarius III's mean metallicity ([Fe/H]) and metallicity dispersion ($\sigma_{[Fe/H]}$) through a nearly identical Bayesian fit to that used for the velocity and velocity dispersion. The observed metallicity distribution of the RGB stars was modeled as a Gaussian with both an intrinsic component and a component associated with observational errors. We assumed a weak uniform prior on Aquarius III's metallicity dispersion of $0 < \sigma_{[Fe/H]} < 2$ and derived posterior probability distributions for each parameter with `emcee` using 100 walkers taking 6000 steps (with the first 1000 discarded as burn-in).

For our primary measurement, we limited our metallicity sample to the six RGB stars with $S/N > 7$ pixel^{-1} spectra. The resulting posterior distributions for this sample are shown in the right-hand panel of Figure 4. From the 16th/84th percentile of the marginalized 1D posteriors, we find a mean metallicity of $[Fe/H] = -2.61 \pm 0.21$ and a metallicity dispersion of $\sigma_{[Fe/H]} = 0.46^{+0.26}_{-0.14}$. If we opted to revise our minimum S/N threshold for metallicities to $S/N > 10$ pixel^{-1} ($S/N > 4$ pixel^{-1}), we find $[Fe/H] = -2.64^{+0.35}_{-0.34}$ and $\sigma_{[Fe/H]} = 0.64^{+0.48}_{-0.24}$ ($[Fe/H] = -2.47 \pm 0.14$ and $\sigma_{[Fe/H]} = 0.39^{+0.15}_{-0.10}$). In short, these tests demonstrate our metallicity results are fairly insensitive to the exact S/N cutoff we applied.

Our primary metallicity and metallicity dispersion constraints are subject to the strong caveat that they are derived from a sample of only six stars. Thus, their magnitudes should be interpreted cautiously. What is nearly certain, however, is that our measured metallicity dispersion is nonzero: the posterior probability distribution derived from the MCMC suggests a lower limit of $\sigma_{[Fe/H]} > 0.25$ at the 95% credible level, clearly indicating that measurement uncertainty alone cannot explain the observed spread. A resolved dispersion persists even if either the most metal-poor star or the most metal-rich star is excluded. This resolved metallicity spread provides strong evidence in favor of a dwarf galaxy classification for Aquarius III (see Section 6.1).

5. Elemental Abundances from Magellan/MagE Spectroscopy

5.1. Observations and Data Reduction

The brightest star in Aquarius III (Gaia DR3 2447566690779941504 in Table 2) is sufficiently bright so as to allow for more detailed spectroscopic investigation of its chemical abundances. On the night of 2023 October 14, we obtained a long-slit spectrum of this star with the the Magellan Echellete (MagE) spectrograph. We used the 1.″0 slit, which provides a resolution of $\mathcal{R} \sim 4100$ over a wavelength range of ~3000–11000 Å. We collected 2×2400 s exposures and 1×1800 s exposure, for a total integration time of 6600 s (1.8 hr). ThAr frames were collected after each science exposure, and Xe-flash flats and quartz flats were taken at the beginning and end of the night. Each exposure was reduced individually using the MagE pipeline provided in the Carnegie Python Distribution (`CarPy`; D. D. Kelson et al. 2000; D. D. Kelson 2003) and subsequently normalized, and the three spectra were then coadded with inverse-variance weighting.

Information-rich wavelength regions of the resultant coadded spectrum are shown in Figure 6, including the ~3850–4400 Å spectral region covering the Ca II H&K lines and CH *G* band as well as the 5100–5300 Å spectral region featuring the Mg I b triplet. Even from visual inspection alone, the strength and width of these features support the classification of the star as a cool, luminous, metal-poor, and likely carbon-enhanced K giant. In the following subsections, we formalize this interpretation through an automated spectral fit as well as through synthesis of several key lines/features.

5.2. Stellar Parameters, Metallicity, and α-abundance

We performed a fit to the star's radial velocity, effective temperature, surface gravity, iron abundance, and α-element abundance from each MagE spectrum using `Payne4MagE`.[47] `Payne4MagE` is an instrument-specific wrapper for The Payne (Y.-S. Ting et al. 2019), which is a neural network-based emulator designed for constructing synthetic stellar spectra given a fixed set of labels (stellar parameters and abundances). For our application here, we simultaneously fit the spectrum from each of the three exposures over the restricted wavelength range of 4700–6700 Å. This intentionally selected for a region of the spectrum redward of the CH *G* band, which was necessary to avoid biasing the fit since the emulator used here was trained on models limited to $[C/Fe] = 0$. Wavelengths redder than 6700 Å in our spectrum primarily consisted of either information-poor continuum or absorption lines not matched well by most spectral synthesis models (e.g., the CaT), and thus, we avoided this regime as well. In the same vein, we also masked several strong absorption lines within the main fit region of ~4700 Å–6700 (including Hα and Hβ).

The best-fitting spectral model from the joint `Payne4MagE` fit to the three exposures was that of a cool giant with $T_{eff} = 4900 \pm 130$ K, $\log(g)/(\mathrm{cm\ s^{-2}}) = 1.9 \pm 0.37$,$[Fe/H] = -3.2 \pm 0.11$, $[\alpha/Fe] = 0.59 \pm 0.07$, where the reported uncertainties were derived from a Gaussian approximation to the empirical covariance matrix.[48] The iron abundance derived from the MagE spectrum and `Payne4MagE` is in excellent agreement with the EW-based CaT metallicity derived from our DEIMOS spectrum of the same star ($[Fe/H] = -3.04 \pm 0.10$). As a third and final independent estimate of the metallicity, we computed the "KP index" of the Ca II K line at 3933.7 Å (T. C. Beers et al. 1990) following a similar procedure to A. Chiti et al. (2018). This EW-based calibration yielded an estimate of $[Fe/H] = -2.89 \pm 0.26$, consistent with both of the other estimates described above. Collectively, these measurements demonstrate that Aquarius III's brightest red giant member is at the boundary of the extremely metal-poor (EMP) regime.

5.3. Carbon and Barium Abundance

A significant fraction of the EMP stars in the Milky Way halo and in ultra-faint dwarf galaxies exhibit an enhancement in carbon (e.g., $\gtrsim$20%–50% below $[Fe/H] = -3.0$ have $[C/Fe] >$ 0.7–1.0; S. Lucatello et al. 2006; Y. S. Lee et al. 2013; V. M. Placco et al. 2014; A. Arentsen et al. 2022). Within the ultra-faint dwarfs in particular, this carbon enhancement is often paired with a deficiency in neutron-capture elements—the so-called CEMP-no pattern (e.g., T. C. Beers & N. Christlieb 2005). The CEMP-no stars in UFDs may be the descendants of faint Population III supernova, and thus, these stars offer an

[47] https://github.com/yupengyao/Payne4MagE

[48] The effective line broadening of the MagE spectrum, which includes the contribution of both the instrumental resolution and the contribution of macroturbulence, was found to be ~20 km s^{-1}.

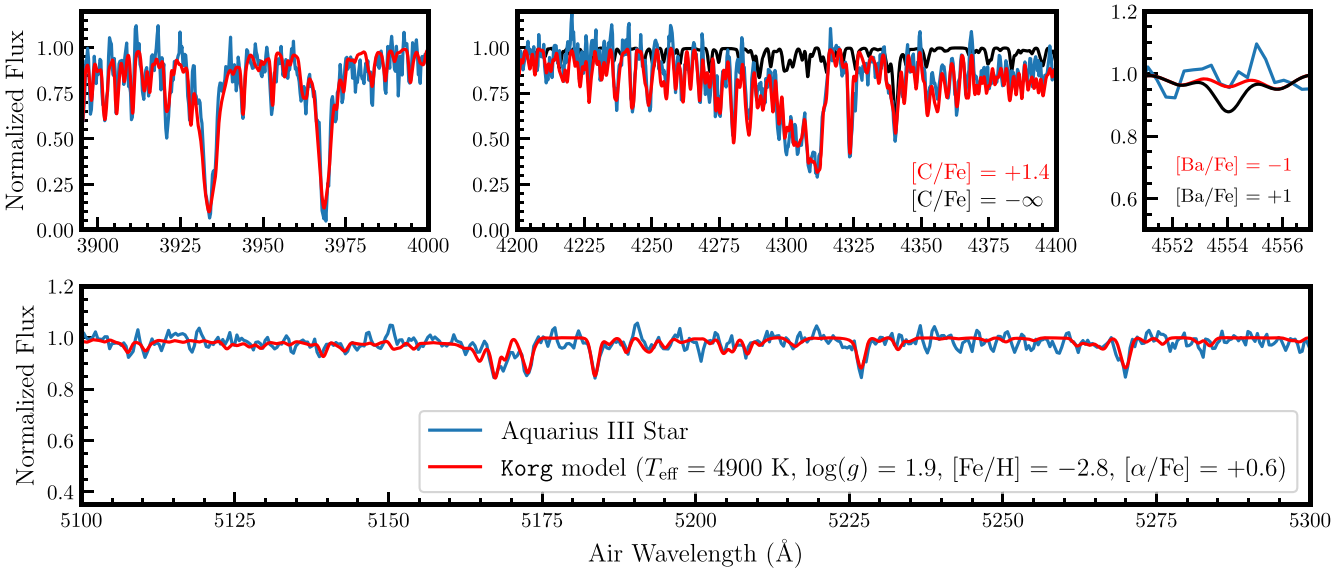

Figure 6. Important wavelength regions of our MagE spectrum for the brightest star in Aquarius III (Gaia DR3 2447566690779941504) compared against a spectral synthesis model from `Korg`. In each panel, the observed spectrum is shown in blue while a matched synthetic spectrum, smoothed to $R = 4100$, is shown in red. Top row, left panel: the Ca II H&K lines. Top row, center panel: the CH G band, compared to a model with [C/Fe] = +1.4 (red) and no carbon (black). Top row, right: narrow wavelength range covering the strong Ba II λ4554 resonance line. A model with [Ba/Fe] = +1 is shown in black. Although the data are noisy, this Ba-enhanced model is clearly disfavored by the nondetection of this line. Bottom panel: the wavelength range 5100–5300 Å, which most notably includes the Mg I b triplet as well as a number of iron lines.

insightful window into the chemical evolution of their host galaxies at early times (e.g., M. Jeon et al. 2021). On the other hand, ∼80% of halo CEMP stars outside known dwarf galaxies are CEMP-*s* stars thought to be the products of mass transfer from an asymptotic giant branch star binary companion (e.g., T. C. Beers & N. Christlieb 2005; W. Aoki et al. 2007).

To test whether Aquarius III's brightest star is carbon enhanced, we compared our observed MagE spectrum against synthetic spectra generated using the Julia-based spectral synthesis package `Korg` (A. J. Wheeler et al. 2023, 2024). `Korg` interpolates from a grid of MARCS model atmospheres and generates synthetic spectra under the assumption of 1D local thermodynamic equilibrium. For our purposes, we adopted a model atmosphere with the temperature and surface gravity from the `Payne4Mage` fit, [M/H] = −2.5 (the lowest available in `Korg`'s MARCS atmosphere grid at the time of our analysis), and [α/Fe] = +0.6. We then synthesized spectra with varied carbon abundances assuming the same $T_{\rm eff}$, log(g), and a marginally higher iron abundance than derived above, [Fe/H] = −2.8, which was found to better match the strength of the observed iron lines. The best-fitting carbon abundance was found to be a model with [C/Fe] = +1.4 for the star assuming this higher metallicity. We then added a 0.08 dex evolutionary correction based on the online calculator associated with V. M. Placco et al. (2014) to account for the surface carbon depletion associated with CN cycling on the RGB.[49] Adopting a conservative of uncertainty of ±0.3 dex motivated by our use of a model atmosphere at a higher metallicity, our final measurement is [C/Fe] = 1.48 ± 0.3. We therefore conclude that the star is consistent with a CEMP classification.

In an attempt to distinguish between the CEMP-s and CEMP-no scenarios for this star, we next explored whether it was possible to measure barium (an *s*-process element) from the Ba II λ4554 line or strontium (a predominantly *r*-process element for metal-poor stars) from the Sr II λ4077 line. We ultimately concluded that a reliable quantitative measurement could not be made from either line due to the low resolution and somewhat low S/N of our MagE spectrum. This being said, we see no evidence for strong absorption at the expected wavelength for any of the strong Ba lines covered by our spectrum (see Figure 6 for the Ba II λ4554 resonance line). The comparison to `Korg` models with varied barium abundances allows us to rule out [Ba/Fe] > +1—excluding the CEMP-s possibility for this star. This lack of *s*-process enhancement therefore favors a CEMP-no classification for this star.

In summary, our MagE spectrum indicates that the brightest star in Aquarius III is a carbon-enhanced, metal-poor star at the boundary of the EMP regime ([Fe/H] ≈ −3) that is most consistent with a CEMP-no classification. Our results derived here from spectral synthesis should be regarded as indicative as opposed to a precise quantitative analysis, and a higher-resolution, higher-S/N spectrum will be necessary to further ascertain this star's nature.

6. Discussion

6.1. Classification of Aquarius III as a Dwarf Galaxy

Recent discoveries of ultra-faint systems in the Milky Way halo have generally fallen into two broad categories: extended, dark-matter-dominated ultra-faint dwarf galaxies and compact, low-luminosity systems generally presumed to be baryon-dominated ultra-faint star clusters. We find that Aquarius III is more consistent with the former class of satellites on the basis of its size and metallicity distribution.

In detail, Aquarius III's physical size of $r_{1/2} = 41^{+9}_{-8}$ pc is larger than all known Milky Way globular clusters (see left panel of Figure 5); even if we adopted the lower bound of our 1σ credible interval, the only comparably extended clusters fall several magnitudes brighter and at much higher surface

[49] https://vplacco.pythonanywhere.com/

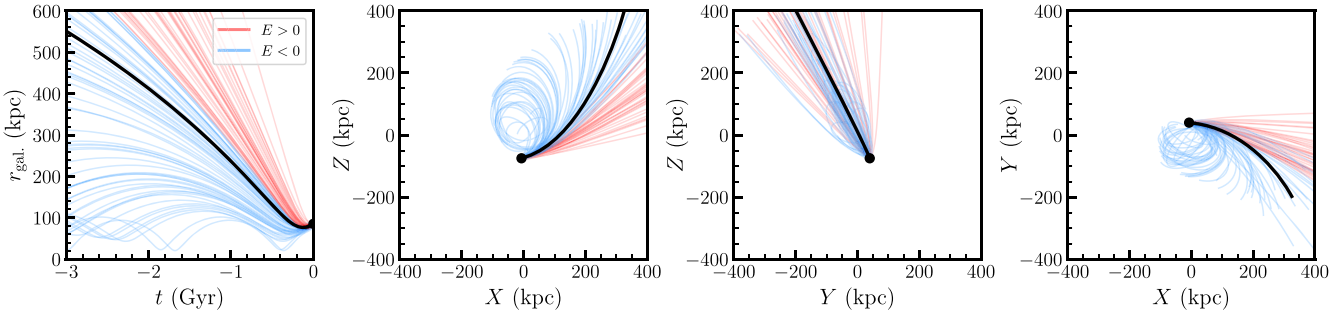

Figure 7. Projections of Aquarius III's orbit for the last 3 Gyr in the P. J. McMillan (2017) Milky Way potential. In each panel, the solid black curve depicts a "fiducial" orbit assuming the median positions and velocities in Table 1, and the blue (red) orbits depict bound (unbound) realizations randomly sampled from our parent sample of 5000 realizations (100 random samples in total). Aquarius III's current position is depicted in each panel by a black point. Left: Galactocentric radius ($r_{gal.}$) vs. time (t), where $t = 0$ denotes the present day. Center left: Galactocentric Z vs. X, i.e., an edge-on view of disk plane. Center right: Galactocentric Z vs. Y. Right: Galactocentric Y vs. X, i.e., the plane parallel to the disk. Note that we have truncated the axis limits in all four panels for sake of visualization.

brightness. With respect to its metallicity distribution, Aquarius III's metallicity dispersion of $\sigma_{[Fe/H]} = 0.46^{+0.26}_{-0.14}$ dex is clearly nonzero. This not only points to multiple generations of star formation in the system but also suggests that Aquarius III inhabits a dark matter halo with a gravitational potential deep enough to retain supernova ejecta (B. Willman & J. Strader 2012). This statement is not in tension with our finding of a low velocity dispersion, as dynamical masses within the half-light radius as large as $5.1 \times 10^5 M_\odot$ are permitted by the current kinematic observations (at the 95% credible level). Lastly, but perhaps least persuasively, we note that Aquarius III's mean metallicity is closely consistent with the expectation from the luminosity–metallicity relation for dwarf galaxies (E. N. Kirby et al. 2013b), and the metallicity of its brightest star—as measured through several independent techniques—is more metal-poor than any known star in any known intact globular cluster. This star's combination of a low barium abundance and strong carbon enhancement also matches the enrichment pattern commonly seen in very-metal-poor ultra-faint dwarf galaxy stars (A. P. Ji et al. 2019).

6.2. Proper Motion and Orbit

The brightest two spectroscopically confirmed members in Aquarius III each have a proper-motion measurement reported in Gaia Data Release 3 (Gaia Collaboration et al. 2016, 2023), enabling us to measure the galaxy's systemic proper motion.[50] We performed a simple two-parameter MCMC fit constraining the Aquarius III's systemic proper motion in R.A. and decl. ($\mu_{\alpha*}$ and μ_δ, respectively) based on the likelihood presented in Equations (3) and (4) of A. B. Pace & T. S. Li (2019). We applied no priors and assumed no intrinsic proper-motion dispersion in either component. Posterior probability distributions for each component were derived using `emcee`, from which we estimated $\mu_{\alpha*} = 1.01 \pm 0.25$ mas yr^{-1} and $\mu_\delta = -0.10 \pm 0.20$ mas yr^{-1}. These estimates and uncertainties account for the covariance between the proper-motion components for a given star; however, we neglected the $\mathcal{O}(0.02$ mas yr$^{-1})$ spatially covariant systematic errors discussed by L. Lindegren et al. (2021) as they are subdominant.

With complete 6D phase-space information in hand, we integrated 5000 realizations of Aquarius III's orbit using the `galpy` Python package (J. Bovy 2015). Initial conditions for these realizations were generated by sampling directly from the posterior probability distributions on each parameter (α, δ, $D_\odot$, μ_α, μ_δ, $v_{hel.}$). For each set of initial conditions, we rewound Aquarius III's orbit for the last 3 Gyr in the static, axisymmetric P. J. McMillan (2017) potential model. This is a six-component model including a bulge, a thin stellar disk and a thick stellar disk, an atomic and molecular gaseous disk, and a Navarro–Frenk–White dark matter halo (J. F. Navarro et al. 1997), all summing to a total virial mass of $1.3 \times 10^{12} M_\odot$. At the conclusion of each integration, we recorded Aquarius III's orbital properties including its orbital eccentricity (e) apocentric and pericentric radii (r_{apo} and r_{peri}, respectively), total orbital energy per unit mass (E_{tot}), and the Z-component of its angular momentum (L_Z). Throughout, we adopted a right-handed Galactocentric coordinate frame with the solar distance from the Galactic center and the corresponding circular velocity set to the properties of the best-fitting potential model from P. J. McMillan (2017), namely, $R_0 = 8.21$ kpc and $v_{circ} = 233.1$ km s^{-1}. We further assumed the solar peculiar motion about the local standard of rest from R. Schönrich et al. (2010).

In Figure 7, we display four different representations of Aquarius III's orbital history for the last 3 Gyr. Each panel shows 100 randomly drawn realizations where realizations corresponding to bound orbits ($E_{tot} < 0$) are shown in blue, and realizations corresponding to unbound orbits ($E_{tot} > 0$) are shown in red. These represent ∼61% and ∼39% of cases, respectively. In black, we also depict a "fiducial" orbit corresponding to the case wherein Aquarius III's present-day phase-space properties were set to be exactly equal to the best-fit values quoted in Table 1. Broadly, our results favor a scenario in which Aquarius III is orbiting retrograde with respect to the Milky Way disk ($L_Z = (13^{+3}_{-5}) \times 10^3$ kpc km s^{-1}, in our right-handed coordinate frame) and has passed its orbital pericenter within the last ∼250 Myr. Aquarius III's Galactocentric radius at this recent pericentric passage is relatively tightly constrained to $r_{peri} = 78 \pm 7$ kpc. By contrast, its orbital apocenter is very poorly constrained: of the 61% of orbits that are bound, about half have no apocentric passages within the last 3 Gyr while the remainder are distributed across a wide range of possible apocenters.

Although our fiducial orbit suggests Aquarius III is a bound satellite, these results are fully consistent with a scenario in

[50] For completeness, the Gaia DR3 proper motions for these two stars are $(1.03 \pm 0.27, -0.20 \pm 0.21)$ mas yr^{-1} and $(1.07 \pm 0.70, 0.48 \pm 0.55)$ mas yr^{-1}. Both stars have high-quality astrometric solutions as quantified by the `fidelity_v2` classifier introduced by J. Rybizki et al. (2022).

which Aquarius III is on the first infall onto the Milky Way, as is believed to the case for a significant fraction of the known ultra-faint dwarfs (J. D. Simon 2018; F. Hammer et al. 2021). The possibility of the first infall led us to explore whether Aquarius III is consistent with having accreted with the Large Magellanic Cloud (LMC) and Small Magellanic Cloud (SMC), which themselves are believed to be on their first infall (G. Besla et al. 2010; N. Kallivayalil et al. 2013). This hypothesis is supported by Aquarius III's projected proximity to the trailing arm of the Magellanic Stream's H I gas component and its 3D proximity to stars comprising the trailing portion of the recently reported "Magellanic Stellar Stream" (MSS; V. Chandra et al. 2023). However, despite this positional similarity, we found that Aquarius III's 3D kinematics are inconsistent with a Magellanic association: its retrograde orbit immediately disfavors an association, and more convincingly, its orbital angular momentum about the Galactocentric Y-axis is clearly inconsistent with that of the claimed MSS debris stars ($L_Y = (24^{+7}_{-8}) \times 10^3$ kpc km s^{-1}, compared to the selection $L_Y < 5 \times 10^3$ kpc km s^{-1} from V. Chandra et al. 2023). This kinematic inconsistency manifests most clearly in the center right panel of Figure 7, where Aquarius III's orbit has it approaching the Milky Way disk from above the disk plane (positive Z), in contrast to the Clouds, which are infalling toward the Milky Way from below the disk plane (negative Z). We conclude that an association between Aquarius III and the LMC/SMC is highly improbable.

This all being said, we caution that our proper-motion measurement is quite uncertain owing to both the small number of stars in Aquarius III with Gaia proper motions (just two) as well as the large proper-motion uncertainties on each of these stars. Furthermore, we note that orbit integrations performed based on uniformly sampling from a proper-motion measurement posterior distribution with large errors can bias orbital history inferences toward the case of an eccentric orbit with the satellite near its pericenter (see Section 5.2 of L. Correa Magnus & E. Vasiliev 2022). This is because these uniformly drawn samples will favor values for the tangential velocity that are *larger* in magnitude than the true tangential velocity, whereas these possible orbits are in reality far less likely to be "sampled" from the host halo's distribution function than bound, low-velocity orbits (L. Correa Magnus & E. Vasiliev 2022). A proper treatment involving weighting samples by the distribution function is beyond the scope of this work, and for now, we simply conclude that improved proper-motion measurements (e.g., from future Gaia data releases) will provide a more precise and accurate constraint on Aquarius III's orbital history. As we describe in the following section, a secure determination of Aquarius III's orbit will be important for interpreting its cold velocity dispersion.

6.3. A Kinematically Cold, Tidally Unscathed Dark Matter Halo for Aquarius III?

One consequence of Aquarius III's plausible first-infall orbital history and large pericenter distance ($r_{\rm peri} = 78 \pm 7$ kpc) is that the galaxy very likely has not experienced significant tidal mass loss induced by the Milky Way disk. This permits the possibility that Aquarius III's low present-day halo mass is a reasonably faithful tracer of its halo mass at the time of its formation, i.e., that it formed in a very-low-mass dark matter halo. This would be a stronger statement than has been previously possible with other faint dwarf satellites with strong velocity dispersion limits—Segue 2, Tucana III, and Draco II ($\sigma_v <$ [2.6, 1.5, 5.9] km s^{-1}, respectively)—all of which display signatures of mass loss or disruption and are situated in the inner halo (E. N. Kirby et al. 2013a; J. D. Simon et al. 2017; N. Longeard et al. 2018). Likewise, three additional ultra-faint dwarfs with strong velocity dispersion upper limits, namely, Grus II, Triangulum II, and Tucana V ($\sigma_v <$ [3.4, 2.0, 3.1] km s^{-1}; J. D. Simon et al. 2020; R. Buttry et al. 2022; T. T. Hansen et al. 2024) each have orbital pericenters that leave them vulnerable to the disk's tidal influence, even if direct evidence for disruption has not yet been observed. In each of these cases—barring Aquarius III—tidal mass loss induced by the Milky Way disk remains a viable explanation for the low observed velocity dispersions. Indeed, for Tucana III, this is a near certainty: N-body simulations suggest that extreme tidal dark matter loss in satellites precedes substantial stellar mass loss (J. Peñarrubia et al. 2008), and thus, the presence of clear tidal tails in Tucana III's stellar component (A. Drlica-Wagner et al. 2016; T. S. Li et al. 2018a) points to severe mass loss in its dark matter component. In short, then, Aquarius III stands alone among the known Milky Way satellite population in that it appears both very kinematically cold and tidally unscathed by the Milky Way disk.

The combination of these properties potentially makes Aquarius III an interesting laboratory for studying galaxy formation physics in low-mass dark matter halos. If its velocity dispersion is confirmed to be $\sigma_v \lesssim 2$ km s^{-1} based on additional kinematic observations, Aquarius III's implied halo mass will likely fall in the low $10^8\,M_\odot$ regime. The galaxy occupation fraction in this regime (and at lower halo masses) is sensitive to the available channels for gas cooling and to the timing of cosmic reionization (e.g., G. Efstathiou 1992; R. S. Somerville 2002; A. Benitez-Llambay & C. Frenk 2020; O. Nebrin et al. 2023), and whether these halos are expected to exist in the first place is sensitive to the nature of dark matter. Put succinctly, confirmation of a galaxy that formed in such a low-mass halo would almost certainly require the need for H_2 cooling and would disfavor cosmological models with early reionization (V. Manwadkar & A. V. Kravtsov 2022; N. Ahvazi et al. 2024). Moreover, such a galaxy would disfavor warm dark matter particle models, which suppress the small-scale power spectrum at masses approaching $\sim 10^8 M_\odot$ (e.g., warm dark matter particles with masses $\lesssim$5 keV). Similar conclusions have previously been drawn at the satellite population level based on abundance matching (e.g., P. Jethwa et al. 2018; E. O. Nadler et al. 2021; O. Newton et al. 2021), but the robust confirmation of an individual nondisrupting galaxy in this halo mass range would be a novel and clean confirmation of these constraints.

One caveat to the above is that it remains possible that Aquarius III has lost mass through "preprocessing" in a *different* group environment prior to infall onto the Milky Way (see, e.g., S. L. McGee et al. 2009; A. R. Wetzel et al. 2013; A. Hou et al. 2014; G. D. Joshi et al. 2019, for useful context), which would complicate the interpretation of its low velocity dispersion. Illustratively, A. R. Wetzel et al. (2015) studied Milky Way/M31-like pairs in the ELVIS simulations and report that ∼50% of satellites of comparable stellar mass to Aquarius III resided in another massive host halo prior to infall. These groups of galaxies/subhalos are commonly disrupted at time of infall (A. R. Wetzel et al. 2015), and thus, we are

fundamentally limited in our ability to assess whether preprocessing has occurred for Aquarius III.

In any case, Aquarius III's status as one of the Milky Way's least massive confirmed satellite galaxies yet identified makes it an appealing target for future follow-up. Specifically, higher-precision radial velocity measurements—ideally from an expanded member sample—are a critical next step before any actual constraints can be made based on Aquarius III's stellar kinematics. Expanding the sample of spectroscopic members will be challenging given that our current Keck/DEIMOS sample already nearly reaches the base of the RGB at $g_0 \sim 23$. However, even a second equal-depth epoch of Keck/DEIMOS observations covering the same members may be sufficient to place a strong enough dispersion limit to settle whether Aquarius III truly is an unprecedentedly low-mass galaxy. A second, high-precision epoch would also enable the identification and removal of short-period spectroscopic binaries, which could be either inflating or deflating the velocity dispersion constraint derived from our current single-epoch data set (e.g., A. W. McConnachie & P. Côté 2010; Q. E. Minor et al. 2010; C. Pianta et al. 2022; W. Wang et al. 2023).

6.4. (Limits on) Astrophysical J-factor

The Milky Way's ultra-faint dwarf satellites are excellent targets in the search for gamma-ray emission associated with annihilating dark matter owing to their high dark matter densities and relatively minimal baryonic components (M. Ackermann et al. 2015; A. Geringer-Sameth et al. 2015b; A. McDaniel et al. 2023; K. K. Boddy et al. 2024). The astrophysical component of the expected signal from dark matter annihilation is quantified in the J-factor (J), which represents the integral over the line of sight of the dark matter density squared:

$$J(\theta) = \iint_{\mathrm{l.o.s}} \rho^2_{\mathrm{DM}}(r)\, d\ell d\Omega,$$

within a solid angle Ω of angular radius θ. The standard method for computing the J-factor is to infer the dark matter density profile by comparing solutions to the spherical Jeans equations to the measured velocity dispersion (e.g., V. Bonnivard et al. 2015; A. Geringer-Sameth et al. 2015a; A. B. Pace & L. E. Strigari 2019). To apply this approach to Aquarius III, we followed the Jeans modeling implementation described by A. B. Pace & L. E. Strigari (2019), which assumes that the velocity anisotropy was constant with radius. Taking a prior on the maximum circular velocity of $v_{\mathrm{max}} > 1$ km s^{-1}, this yielded an estimate for Aquarius III's J-factor within a solid angle of radius $\theta = 0.^{\circ}5$ (hereafter $J(0.^{\circ}5)$) of $\log 10(J(0.^{\circ}5)/(\mathrm{GeV}^2\ \mathrm{cm}^{-5}) < 17.7$. As a simple check on this result, we also estimated Aquarius III's J-factor using the empirical scaling relation from A. B. Pace & L. E. Strigari (2019):

$$\frac{J(0.^{\circ}5)}{\mathrm{GeV}^2\ \mathrm{cm}^{-5}} \approx 10^{17.87}\left(\frac{\sigma_v}{5\ \mathrm{km\ s}^{-1}}\right)^4\left(\frac{D_{\odot}}{100\ \mathrm{kpc}}\right)^{-2}\left(\frac{r_{1/2}}{100\ \mathrm{pc}}\right)^{-1}.$$

Neglecting uncertainties on this relation itself, this calculation yielded an upper limit on Aquarius III's logarithmic J-factor of $\log 10(J(0.5)/(\mathrm{GeV}^2\ \mathrm{cm}^{-5}) < 17.8$ in good agreement with the full Jeans modeling treatment.

Owing to Aquarius III's small velocity dispersion and large distance, this upper limit on the galaxy's estimated J-factor is quite stringent and places Aquarius III in the bottom third of ultra-faint dwarf galaxy J-factors (see, e.g., Figure 11 of M. E. Heiger et al. 2024). We therefore conclude that Aquarius III will not meaningfully contribute to indirect-detection constraints even within the context of stacked analyses.

7. Summary and Conclusions

We have presented the discovery of Aquarius III, a low-luminosity Milky Way halo satellite identified in DECam imaging data processed by DELVE. Follow-up imaging from DECam clearly established it as a bona fide ultra-faint stellar system in the outer Milky Way halo. Multiobject spectroscopy from Keck/DEIMOS then enabled measurement of its stellar kinematics and metallicity distribution from a parent sample of 11 member stars, affirming its nature as a metal-poor dwarf galaxy—albeit a low-mass one with no currently resolvable velocity dispersion. An additional long-slit spectrum of Aquarius III's brightest star from Magellan/MagE revealed it to be a carbon-enhanced, α-element-enhanced, extremely metal-poor star worthy of follow-up with higher-resolution spectroscopy. Gaia proper motions for Aquarius III's two brightest stars allowed us to explore its orbital history, from which we concluded that the galaxy is on a retrograde orbit having recently passed its pericenter in the outer halo. Lastly, we synthesized the sum total of these measurements to argue that Aquarius III may represent a clean example of a galaxy that formed in a halo at $M_{\mathrm{peak}} \sim 10^8 M_{\odot}$—a hypothesis that can be tested with additional spectroscopic observations.

Looking to the future, the unprecedentedly deep, wide-field data from the upcoming Vera C. Rubin Observatory and its Legacy Survey of Space and Time will yield a deluge of dozens to hundreds of faint Local Group satellites in the southern sky (e.g., J. R. Hargis et al. 2014; O. Newton et al. 2018; V. Manwadkar & A. V. Kravtsov 2022). Aquarius III is, in many ways, emblematic of the Milky Way dwarf satellites that Rubin will discover in great number: low-luminosity, distant galaxies with at most a few dozen red giant branch stars (see, e.g., Figures 8 and 9 of J. D. Simon 2019). Spectroscopically characterizing these systems is costly—here, for example, requiring a half night on a 10 m class telescope—yet these data are indispensable for measuring their dynamical masses and metallicities and thereby solidly establishing their classifications as dwarf galaxies. We therefore emphasize that capitalizing on these discoveries from Rubin will require a major investment of time on large-aperture telescopes for multiobject spectroscopy. Only with these data can we maximize these galaxies' utility as laboratories for testing models of galaxy formation and the small-scale structure predictions of ΛCDM cosmology.

Acknowledgments

This material is based upon work supported by the National Science Foundation under grants AST-2108168, AST-2108169, AST-2307126, and AST-2407526. This material is based upon work supported by the National Science Foundation Graduate Research Fellowship Program under grant No. DGE-2139841. Any opinions, findings, and conclusions or recommendations expressed in this material are those of the

author(s) and do not necessarily reflect the views of the National Science Foundation. This project is partially supported by the NASA Fermi Guest Investigator Program Cycle 9 No. 91201. This work is partially supported by Fermilab LDRD project L2019-011.

W.C. gratefully acknowledges support from a Gruber Science Fellowship at Yale University. D.J.S. acknowledges support from NSF grants AST-1821967, 1813708, and AST-2205863. J.L.C. acknowledges support from NSF grant AST-1816196. G.E.M. acknowledges support from the University of Toronto Arts & Science Post-doctoral Fellowship program, the Dunlap Institute, and the Natural Sciences and Engineering Research Council of Canada (NSERC) through grant RGPIN-2022-04794. J.A.C.-B. acknowledges support from FONDECYT Regular N 1220083. C.E.M.-V. is supported by the international Gemini Observatory, a program of NSF NOIRLab, which is managed by the Association of Universities for Research in Astronomy (AURA) under a cooperative agreement with the U.S. National Science Foundation, on behalf of the Gemini partnership of Argentina, Brazil, Canada, Chile, the Republic of Korea, and the United States of America. A.B.P. acknowledges support from NSF grant AST-1813881. I.U.R. acknowledges support from the NASA Astrophysics Data Analysis Program grant No. 80NSSC21K0627, and the NSF grant AST 2205847.

Some of the data presented herein were obtained at Keck Observatory, which is a private 501(c)3 nonprofit organization operated as a scientific partnership among the California Institute of Technology, the University of California, and the National Aeronautics and Space Administration. The Observatory was made possible by the generous financial support of the W. M. Keck Foundation. The authors wish to recognize and acknowledge the very significant cultural role and reverence that the summit of Maunakea has always had within the Native Hawaiian community. We are most fortunate to have the opportunity to conduct observations from this mountain. This research has also made use of the Keck Observatory Archive (KOA), which is operated by the W. M. Keck Observatory and the NASA Exoplanet Science Institute (NExScI), under contract with the National Aeronautics and Space Administration.

This paper includes data gathered with the 6.5 m Magellan Telescopes located at Las Campanas Observatory, Chile. This project used data obtained with the Dark Energy Camera, which was constructed by the Dark Energy Survey (DES) collaboration. Funding for the DES Projects has been provided by the DOE and NSF (USA), MISE (Spain), STFC (UK), HEFCE (UK), NCSA (UIUC), KICP (U. Chicago), CCAPP (Ohio State), MIFPA (Texas A&M University), CNPQ, FAPERJ, FINEP (Brazil), MINECO (Spain), DFG (Germany), and the collaborating institutions in the Dark Energy Survey, which are Argonne Lab, UC Santa Cruz, University of Cambridge, CIEMAT-Madrid, University of Chicago, University College London, DES-Brazil Consortium, University of Edinburgh, ETH Zürich, Fermilab, University of Illinois, ICE (IEEC-CSIC), IFAE Barcelona, Lawrence Berkeley Lab, LMU München, and the associated Excellence Cluster Universe, University of Michigan, NSF's National Optical-Infrared Astronomy Research Laboratory, University of Nottingham, Ohio State University, OzDES Membership Consortium, University of Pennsylvania, University of Portsmouth, SLAC National Lab, Stanford University, University of Sussex, and Texas A&M University.

Based on observations at NSF Cerro Tololo Inter-American Observatory, NSF NOIRLab (NOIRLab prop. ID 2019A-0305; PI: Drlica-Wagner), which is managed by the Association of Universities for Research in Astronomy (AURA) under a cooperative agreement with the U.S. National Science Foundation.

The Legacy Surveys consist of three individual and complementary projects: the Dark Energy Camera Legacy Survey (DECaLS; proposal ID 2014B-0404; PIs: David Schlegel and Arjun Dey), the Beijing-Arizona Sky Survey (BASS; NOAO prop. ID 2015A-0801; PIs: Zhou Xu and Xiaohui Fan), and the Mayall z-band Legacy Survey (MzLS; prop. ID 2016A-0453; PI: Arjun Dey). DECaLS, BASS, and MzLS together include data obtained, respectively, at the Blanco telescope, Cerro Tololo Inter-American Observatory, NSF's NOIRLab; the Bok telescope, Steward Observatory, University of Arizona; and the Mayall telescope, Kitt Peak National Observatory, NOIRLab. Pipeline processing and analyses of the data were supported by NOIRLab and the Lawrence Berkeley National Laboratory (LBNL). The Legacy Surveys project is honored to be permitted to conduct astronomical research on Iolkam Du'ag (Kitt Peak), a mountain with particular significance to the Tohono O'odham Nation.

NOIRLab is operated by the Association of Universities for Research in Astronomy (AURA) under a cooperative agreement with the National Science Foundation. LBNL is managed by the Regents of the University of California under contract to the U.S. Department of Energy.

BASS is a key project of the Telescope Access Program (TAP), which has been funded by the National Astronomical Observatories of China, the Chinese Academy of Sciences (the Strategic Priority Research Program "The Emergence of Cosmological Structures," grant No. XDB09000000), and the Special Fund for Astronomy from the Ministry of Finance. The BASS is also supported by the External Cooperation Program of Chinese Academy of Sciences (grant No. 114A11KYSB20160057), and Chinese National Natural Science Foundation (grant Nos. 12120101003 and 11433005).

The Legacy Survey team makes use of data products from the Near-Earth Object Wide-field Infrared Survey Explorer (NEOWISE), which is a project of the Jet Propulsion Laboratory/California Institute of Technology. NEOWISE is funded by the National Aeronautics and Space Administration.

The Legacy Surveys imaging of the DESI footprint is supported by the Director, Office of Science, Office of High Energy Physics of the U.S. Department of Energy under contract No. DE-AC02-05CH1123, by the National Energy Research Scientific Computing Center, a DOE Office of Science User Facility under the same contract; and by the U.S. National Science Foundation, Division of Astronomical Sciences under contract No. AST-0950945 to NOAO.

This work has made use of data from the European Space Agency (ESA) mission Gaia (https://www.cosmos.esa.int/gaia), processed by the Gaia Data Processing and Analysis Consortium (DPAC, https://www.cosmos.esa.int/web/gaia/dpac/consortium). Funding for the DPAC has been provided by national institutions, in particular the institutions participating in the Gaia Multilateral Agreement.

This work made use of Astropy (https://www.astropy.org): a community-developed core Python package and an ecosystem of tools and resources for astronomy.

This work has made use of the Local Volume Database (https://github.com/apace7/local_volume_database).

This manuscript has been authored by Fermi Research Alliance, LLC, under contract No. DE-AC02-07CH11359 with the US Department of Energy, Office of Science, Office of High Energy Physics. The United States Government retains and the publisher, by accepting the article for publication, acknowledges that the United States Government retains a nonexclusive, paid-up, irrevocable, worldwide license to publish or reproduce the published form of this manuscript, or allow others to do so, for United States Government purposes.

Facilities: Blanco, Gaia, Keck:II (DEIMOS).

Software: `numpy` (S. van der Walt et al. 2011; C. R. Harris et al. 2020), `scipy` (P. Virtanen et al. 2020), `emcee` (D. Foreman-Mackey et al. 2013), `HEALPix` (https://healpix.sourceforge.io; K. M. Górski et al. 2005), `healpy` (A. Zonca et al. 2019), `ugali` (https://github.com/DarkEnergySurvey/ugali; K. Bechtol et al. 2015), `ChainConsumer` (S. R. Hinton 2019), `simple` (A. Drlica-Wagner et al. 2015; K. Bechtol et al. 2015), `astropy` (Astropy Collaboration et al. 2013, 2018, 2022), `Julia` (J. Bezanson et al. 2014), `Korg` (A. J. Wheeler et al. 2024).

Data Availability

All code and data products associated with this work are archived on Zenodo at doi:10.5281/zenodo.14027425. This repository includes our deeper DECam catalog derived from image-level coadds, our DEIMOS spectroscopic catalog including both members and nonmembers and an expanded range of columns, our fully reduced and normalized MagE spectrum, and all MCMC chains produced by our analyses here. The raw DEIMOS spectra are available through the Keck Observatory archive (koa.ipac.caltech.edu/cgi-bin/KOA/nphKOAlogin).

Appendix
References for Data in Figure 5

Figure 5 presents a comparison between Aquarius III's properties and those of the Milky Way's globular clusters, satellite dwarf galaxies, and ultra-faint compact satellites (which may include both star clusters and dwarf galaxies). The measurements in this figure were adopted from the Local Volume Database (A. Pace et al. 2024). The underlying individual references are as follows:

The dwarf galaxy measurements reported in the Local Volume Database version used here were compiled from individual studies including J. D. Simon & M. Geha (2007), M. Mateo et al. (2008), J. L. Carlin et al. (2009), M. Correnti et al. (2009), M. G. Walker et al. (2009), B. Willman et al. (2011), J. D. Simon et al. (2011), S. E. Koposov et al. (2011), E. N. Kirby et al. (2013a), M. G. Walker et al. (2015a), S. E. Koposov et al. (2015a), M. G. Walker et al. (2015b), S. E. Koposov et al. (2015b), A. Drlica-Wagner et al. (2015), E. N. Kirby et al. (2015), J. D. Simon et al. (2015), G. Torrealba et al. (2016a), D. Kim et al. (2016a), G. Torrealba et al. (2016b), A. Drlica-Wagner et al. (2016), D. Crnojević et al. (2016), E. N. Kirby et al. (2017), J. D. Simon et al. (2017), M. E. Spencer et al. (2017), T. S. Li et al. (2017, 2018b), B. Mutlu-Pakdil et al. (2018), D. Homma et al. (2018), G. Torrealba et al. (2018), M. E. Spencer et al. (2018), N. Longeard et al. (2018), R. R. Muñoz et al. (2018), S. E. Koposov et al. (2018), Y. Choi et al. (2018), D. Homma et al. (2019), J. D. Simon (2019), M. Y. Wang et al. (2019), T. K. Fritz et al. (2019), A. B. Pace et al. (2020), A. G. Moskowitz & M. G. Walker (2020), J. D. Simon et al. (2020), S. Mau et al. (2020), W. Cerny et al. (2021a, 2021b), A. Chiti et al. (2021), A. P. Ji et al. (2021), S. A. Cantu et al. (2021), S. A. Jenkins et al. (2021), A. Chiti et al. (2022), H. Richstein et al. (2022), S. E. T. Smith et al. (2023b), W. Cerny et al. (2023b, 2023c), A. Chiti et al. (2023), D. Homma et al. (2023), J. Bruce et al. (2023), H. Richstein et al. (2024), M. E. Heiger et al. (2024), and T. T. Hansen et al. (2024).

Globular cluster measurements were primarily drawn from the compilations of H. Baumgardt & M. Hilker (2018) for structural parameters and H. Baumgardt et al. (2020) for absolute magnitudes. Other measurements for select individual globular clusters were taken from W. E. Harris (1996, 2010 edition), A. Rosenberg et al. (1998), H. A. Kobulnicky et al. (2005), J. Strader & H. A. Kobulnicky (2008), R. Kurtev et al. (2008), K. M. Hamren et al. (2013), D. R. Weisz et al. (2016), M. Gieles et al. (2021), C. Pallanca et al. (2023), S. Leanza et al. (2024), and H. Richstein et al. (2024).

Data for the ultra-faint compact satellites (roughly defined here as halo systems with $M_V \gtrsim -3.5$, $r_{1/2} < 15$ pc) were taken from R. Fadely et al. (2011), E. Balbinot et al. (2013), D. Kim & H. Jerjen (2015b), D. Kim et al. (2015, 2016b), N. F. Martin et al. (2016), B. C. Conn et al. (2018), E. Luque et al. (2018), R. R. Muñoz et al. (2018), D. Homma et al. (2019), G. Torrealba et al. (2019), N. Longeard et al. (2019), S. Mau et al. (2020), W. Cerny et al. (2021a), M. Gatto et al. (2022), W. Cerny et al. (2023a, 2023b), and S. E. T. Smith et al. (2024).

ORCID iDs

W. Cerny https://orcid.org/0000-0003-1697-7062
A. Chiti https://orcid.org/0000-0002-7155-679X
M. Geha https://orcid.org/0000-0002-7007-9725
B. Mutlu-Pakdil https://orcid.org/0000-0001-9649-4815
A. Drlica-Wagner https://orcid.org/0000-0001-8251-933X
C. Y. Tan https://orcid.org/0000-0003-0478-0473
M. Adamów https://orcid.org/0000-0002-6904-359X
A. B. Pace https://orcid.org/0000-0002-6021-8760
J. D. Simon https://orcid.org/0000-0002-4733-4994
D. J. Sand https://orcid.org/0000-0003-4102-380X
A. P. Ji https://orcid.org/0000-0002-4863-8842
T. S. Li https://orcid.org/0000-0002-9110-6163
A. K. Vivas https://orcid.org/0000-0003-4341-6172
E. F. Bell https://orcid.org/0000-0002-5564-9873
J. L. Carlin https://orcid.org/0000-0002-3936-9628
J. A. Carballo-Bello https://orcid.org/0000-0002-3690-105X
A. Chaturvedi https://orcid.org/0000-0001-5143-1255
Y. Choi https://orcid.org/0000-0003-1680-1884
A. Doliva-Dolinsky https://orcid.org/0000-0001-9775-9029
O. Y. Gnedin https://orcid.org/0000-0001-9852-9954
G. Limberg https://orcid.org/0000-0002-9269-8287
C. E. Martínez-Vázquez https://orcid.org/0000-0002-9144-7726
S. Mau https://orcid.org/0000-0003-3519-4004
G. E. Medina https://orcid.org/0000-0003-0105-9576

M. Navabi https://orcid.org/0000-0001-9438-5228
N. E. D. Noël https://orcid.org/0000-0002-8282-469X
V. M. Placco https://orcid.org/0000-0003-4479-1265
A. H. Riley https://orcid.org/0000-0001-5805-5766
I. U. Roederer https://orcid.org/0000-0001-5107-8930
G. S. Stringfellow https://orcid.org/0000-0003-1479-3059
C. R. Bom https://orcid.org/0000-0003-4383-2969
P. S. Ferguson https://orcid.org/0000-0001-6957-1627
D. J. James https://orcid.org/0000-0001-5160-4486
P. Massana https://orcid.org/0000-0002-8093-7471
D. L. Nidever https://orcid.org/0000-0002-1793-3689
J. D. Sakowska https://orcid.org/0000-0002-1594-1466
L. Santana-Silva https://orcid.org/0000-0003-3402-6164
N. F. Sherman https://orcid.org/0000-0001-5399-0114
E. J. Tollerud https://orcid.org/0000-0002-9599-310X

References

Abbott, T. M. C., Adamów, M., Aguena, M., et al. 2021, ApJS, 255, 20
Ackermann, M., Albert, A., Anderson, B., et al. 2015, PhRvL, 115, 231301
Ahvazi, N., Benson, A., Sales, L. V., et al. 2024, MNRAS, 529, 3387
Aoki, W., Beers, T. C., Christlieb, N., et al. 2007, ApJ, 655, 492
Applebaum, E., Brooks, A. M., Christensen, C. R., et al. 2021, ApJ, 906, 96
Arentsen, A., Placco, V. M., Lee, Y. S., et al. 2022, MNRAS, 515, 4082
Astropy Collaboration, Price-Whelan, A. M., Lim, P. L., et al. 2022, ApJ, 935, 167
Astropy Collaboration, Price-Whelan, A. M., Sipőcz, B. M., et al. 2018, AJ, 156, 123
Astropy Collaboration, Robitaille, T. P., Tollerud, E. J., et al. 2013, A&A, 558, A33
Balbinot, E., Santiago, B. X., da Costa, L., et al. 2013, ApJ, 767, 101
Battaglia, G., & Starkenburg, E. 2012, A&A, 539, A123
Baumgardt, H., & Hilker, M. 2018, MNRAS, 478, 1520
Baumgardt, H., Sollima, A., & Hilker, M. 2020, PASA, 37, e046
Bechtol, K., Drlica-Wagner, A., Balbinot, E., et al. 2015, ApJ, 807, 50
Beers, T. C., & Christlieb, N. 2005, ARA&A, 43, 531
Beers, T. C., Preston, G. W., Shectman, S. A., & Kage, J. A. 1990, AJ, 100, 849
Belokurov, V., Zucker, D. B., Evans, N. W., et al. 2006, ApJL, 647, L111
Benitez-Llambay, A., & Frenk, C. 2020, MNRAS, 498, 4887
Besla, G., Kallivayalil, N., Hernquist, L., et al. 2010, ApJL, 721, L97
Bezanson, J., Edelman, A., Karpinski, S., & Shah, V. B. 2014, arXiv:1411.1607
Boddy, K. K., Carter, Z. J., Kumar, J., et al. 2024, PhRvD, 109, 103007
Bonnivard, V., Combet, C., Daniel, M., et al. 2015, MNRAS, 453, 849
Bovy, J. 2015, ApJS, 216, 29
Bressan, A., Marigo, P., Girardi, L., et al. 2012, MNRAS, 427, 127
Bruce, J., Li, T. S., Pace, A. B., et al. 2023, ApJ, 950, 167
Bullock, J. S., & Boylan-Kolchin, M. 2017, ARA&A, 55, 343
Buttry, R., Pace, A. B., Koposov, S. E., et al. 2022, MNRAS, 514, 1706
Cantu, S. A., Pace, A. B., Marshall, J., et al. 2021, ApJ, 916, 81
Carlin, J. L., Grillmair, C. J., Muñoz, R. R., Nidever, D. L., & Majewski, S. R. 2009, ApJL, 702, L9
Carrera, R., Pancino, E., Gallart, C., & del Pino, A. 2013, MNRAS, 434, 1681
Cerny, W., Drlica-Wagner, A., Li, T. S., et al. 2023a, ApJL, 953, L21
Cerny, W., Martínez-Vázquez, C. E., Drlica-Wagner, A., et al. 2022, arXiv:2209.12422
Cerny, W., Martínez-Vázquez, C. E., Drlica-Wagner, A., et al. 2023b, ApJ, 953, 1
Cerny, W., Pace, A. B., Drlica-Wagner, A., et al. 2021a, ApJ, 910, 18
Cerny, W., Pace, A. B., Drlica-Wagner, A., et al. 2021b, ApJL, 920, L44
Cerny, W., Simon, J. D., Li, T. S., et al. 2023c, ApJ, 942, 111
Chandra, V., Naidu, R. P., Conroy, C., et al. 2023, ApJ, 956, 110
Chen, Y., Bressan, A., Girardi, L., et al. 2015, MNRAS, 452, 1068
Chen, Y., Girardi, L., Bressan, A., et al. 2014, MNRAS, 444, 2525
Chiti, A., Frebel, A., Ji, A. P., et al. 2023, AJ, 165, 55
Chiti, A., Frebel, A., Simon, J. D., et al. 2021, NatAs, 5, 392
Chiti, A., Simon, J. D., Frebel, A., et al. 2018, ApJ, 856, 142
Chiti, A., Simon, J. D., Frebel, A., et al. 2022, ApJ, 939, 41
Choi, Y., Nidever, D. L., Olsen, K., et al. 2018, ApJ, 869, 125
Conn, B. C., Jerjen, H., Kim, D., & Schirmer, M. 2018, ApJ, 852, 68
Correa Magnus, L., & Vasiliev, E. 2022, MNRAS, 511, 2610
Correnti, M., Bellazzini, M., & Ferraro, F. R. 2009, MNRAS, 397, L26
Crnojević, D., Sand, D. J., Zaritsky, D., et al. 2016, ApJL, 824, L14
Dey, A., Schlegel, D. J., Lang, D., et al. 2019, AJ, 157, 168
Drlica-Wagner, A., Bechtol, K., Allam, S., et al. 2016, ApJL, 833, L5
Drlica-Wagner, A., Bechtol, K., Mau, S., et al. 2020, ApJ, 893, 47
Drlica-Wagner, A., Bechtol, K., Rykoff, E. S., et al. 2015, ApJ, 813, 109
Drlica-Wagner, A., Carlin, J. L., Nidever, D. L., et al. 2021, ApJS, 256, 2
Drlica-Wagner, A., Ferguson, P. S., Adamów, M., et al. 2022, ApJS, 261, 38
Efstathiou, G. 1992, MNRAS, 256, 43P
Esteban, I., Peter, A. H. G., & Kim, S. Y. 2023, arXiv:2306.04674
Faber, S. M., Phillips, A. C., Kibrick, R. I., et al. 2003, Proc. SPIE, 4841, 1657
Fadely, R., Willman, B., Geha, M., et al. 2011, AJ, 142, 88
Flaugher, B., Diehl, H. T., Honscheid, K., et al. 2015, AJ, 150, 150
Foreman-Mackey, D., Hogg, D. W., Lang, D., & Goodman, J. 2013, PASP, 125, 306
Fritz, T. K., Carrera, R., Battaglia, G., & Taibi, S. 2019, A&A, 623, A129
Fu, S. W., Weisz, D. R., Starkenburg, E., et al. 2023, ApJ, 958, 167
Gaia Collaboration, Prusti, T., de Bruijne, J. H. J., et al. 2016, A&A, 595, A1
Gaia Collaboration, Vallenari, A., Brown, A. G. A., et al. 2023, A&A, 674, A1
Gatto, M., Bellazzini, M., Tortora, C., et al. 2023, arXiv:2311.06037
Gatto, M., Ripepi, V., Bellazzini, M., et al. 2022, ApJL, 929, L21
Geringer-Sameth, A., Koushiappas, S. M., & Walker, M. 2015a, ApJ, 801, 74
Geringer-Sameth, A., Koushiappas, S. M., & Walker, M. G. 2015b, PhRvD, 91, 083535
Gieles, M., Erkal, D., Antonini, F., Balbinot, E., & Penarrubia, J. 2021, NatAs, 5, 957
Górski, K. M., Hivon, E., Banday, A. J., et al. 2005, ApJ, 622, 759
Griffen, B. F., Ji, A. P., Dooley, G. A., et al. 2016, ApJ, 818, 10
Gullikson, K., Dodson-Robinson, S., & Kraus, A. 2014, AJ, 148, 53
Hammer, F., Wang, J., Pawlowski, M. S., et al. 2021, ApJ, 922, 93
Hamren, K. M., Smith, G. H., Guhathakurta, P., et al. 2013, AJ, 146, 116
Hansen, T. T., Simon, J. D., Li, T. S., et al. 2024, ApJ, 968, 21
Hargis, J. R., Willman, B., & Peter, A. H. G. 2014, ApJL, 795, L13
Harris, C. R., Millman, K. J., van der Walt, S. J., et al. 2020, Natur, 585, 357
Harris, W. E. 1996, AJ, 112, 1487
Hartley, W. G., Choi, A., Amon, A., et al. 2021, MNRAS, 509, 3547
Heiger, M. E., Li, T. S., Pace, A. B., et al. 2024, ApJ, 961, 234
Hinton, S. R., 2019 ChainConsumer: Corner plots, LaTeX tables and plotting walks, Astrophysics Source Code Library, ascl:1910.017
Homma, D., Chiba, M., Komiyama, Y., et al. 2019, PASJ, 71, 94
Homma, D., Chiba, M., Komiyama, Y., et al. 2023, arXiv:2311.05439
Homma, D., Chiba, M., Okamoto, S., et al. 2018, PASJ, 70, S18
Hou, A., Parker, L. C., & Harris, W. E. 2014, MNRAS, 442, 406
Husser, T. O., Wende-von Berg, S., Dreizler, S., et al. 2013, A&A, 553, A6
Jenkins, S. A., Li, T. S., Pace, A. B., et al. 2021, ApJ, 920, 92
Jeon, M., Bromm, V., Besla, G., Yoon, J., & Choi, Y. 2021, MNRAS, 502, 1
Jethwa, P., Erkal, D., & Belokurov, V. 2018, MNRAS, 473, 2060
Ji, A. P., Koposov, S. E., Li, T. S., et al. 2021, ApJ, 921, 32
Ji, A. P., Simon, J. D., Frebel, A., Venn, K. A., & Hansen, T. T. 2019, ApJ, 870, 83
Jones, M. G., Mutlu-Pakdil, B., Sand, D. J., et al. 2023, ApJL, 957, L5
Joshi, G. D., Parker, L. C., Wadsley, J., & Keller, B. W. 2019, MNRAS, 483, 235
Kallivayalil, N., van der Marel, R. P., Besla, G., Anderson, J., & Alcock, C. 2013, ApJ, 764, 161
Kauffmann, G., White, S. D. M., & Guiderdoni, B. 1993, MNRAS, 264, 201
Kelson, D. D. 2003, PASP, 115, 688
Kelson, D. D., Illingworth, G. D., van Dokkum, P. G., & Franx, M. 2000, ApJ, 531, 159
Kim, D., & Jerjen, H. 2015a, ApJL, 808, L39
Kim, D., & Jerjen, H. 2015b, ApJ, 799, 73
Kim, D., Jerjen, H., Geha, M., et al. 2016a, ApJ, 833, 16
Kim, D., Jerjen, H., Mackey, D., Da Costa, G. S., & Milone, A. P. 2016b, ApJ, 820, 119
Kim, D., Jerjen, H., Milone, A. P., Mackey, D., & Da Costa, G. S. 2015, ApJ, 803, 63
Kim, S. Y., Peter, A. H. G., & Hargis, J. R. 2018, PhRvL, 121, 211302
Kirby, E. N., Boylan-Kolchin, M., Cohen, J. G., et al. 2013a, ApJ, 770, 16
Kirby, E. N., Cohen, J. G., Guhathakurta, P., et al. 2013b, ApJ, 779, 102
Kirby, E. N., Cohen, J. G., Simon, J. D., et al. 2017, ApJ, 838, 83
Kirby, E. N., Simon, J. D., & Cohen, J. G. 2015, ApJ, 810, 56
Kleyna, J. T., Wilkinson, M. I., Evans, N. W., & Gilmore, G. 2005, ApJL, 630, L141
Klypin, A., Kravtsov, A. V., Valenzuela, O., & Prada, F. 1999, ApJ, 522, 82
Kobulnicky, H. A., Monson, A. J., Buckalew, B. A., et al. 2005, AJ, 129, 239
Koposov, S. E., Belokurov, V., Torrealba, G., & Evans, N. W. 2015a, ApJ, 805, 130

Koposov, S. E., Casey, A. R., Belokurov, V., et al. 2015b, ApJ, 811, 62
Koposov, S. E., Gilmore, G., Walker, M. G., et al. 2011, ApJ, 736, 146
Koposov, S. E., Walker, M. G., Belokurov, V., et al. 2018, MNRAS, 479, 5343
Koposov, S. E., Yoo, J., Rix, H.-W., et al. 2009, ApJ, 696, 2179
Kurtev, R., Ivanov, V. D., Borissova, J., & Ortolani, S. 2008, A&A, 489, 583
Leanza, S., Pallanca, C., Ferraro, F. R., et al. 2024, arXiv:2405.13558
Lee, Y. S., Beers, T. C., Masseron, T., et al. 2013, AJ, 146, 132
Li, T. S., Simon, J. D., Drlica-Wagner, A., et al. 2017, ApJ, 838, 8
Li, T. S., Simon, J. D., Kuehn, K., et al. 2018a, ApJ, 866, 22
Li, T. S., Simon, J. D., Pace, A. B., et al. 2018b, ApJ, 857, 145
Lindegren, L., Klioner, S. A., Hernández, J., et al. 2021, A&A, 649, A2
Longeard, N., Martin, N., Ibata, R. A., et al. 2019, MNRAS, 490, 1498
Longeard, N., Martin, N., Starkenburg, E., et al. 2018, MNRAS, 480, 2609
Lucatello, S., Beers, T. C., Christlieb, N., et al. 2006, ApJL, 652, L37
Luque, E., Santiago, B., Pieres, A., et al. 2018, MNRAS, 478, 2006
Macciò, A. V., Kang, X., Fontanot, F., et al. 2010, MNRAS, 402, 1995
Manwadkar, V., & Kravtsov, A. V. 2022, MNRAS, 516, 3944
Martin, N. F., de Jong, J. T. A., & Rix, H.-W. 2008, ApJ, 684, 1075
Martin, N. F., Ibata, R. A., Chapman, S. C., Irwin, M., & Lewis, G. F. 2007, MNRAS, 380, 281
Martin, N. F., Jungbluth, V., Nidever, D. L., et al. 2016, ApJL, 830, L10
Martínez-Delgado, D., Karim, N., Charles, E. J. E., et al. 2022, MNRAS, 509, 16
Mateo, M., Olszewski, E. W., & Walker, M. G. 2008, ApJ, 675, 201
Mau, S., Cerny, W., Pace, A. B., et al. 2020, ApJ, 890, 136
Mau, S., Nadler, E. O., Wechsler, R. H., et al. 2022, ApJ, 932, 128
McConnachie, A. W., & Côté, P. 2010, ApJL, 722, L209
McDaniel, A., Ajello, M., Karwin, C. M., et al. 2023, arXiv:2311.04982
McGee, S. L., Balogh, M. L., Bower, R. G., Font, A. S., & McCarthy, I. G. 2009, MNRAS, 400, 937
McMillan, P. J. 2017, MNRAS, 465, 76
McQuinn, K. B. W., Mao, Y.-Y., Buckley, M. R., et al. 2023a, ApJ, 944, 14
McQuinn, K. B. W., Mao, Y.-Y., Cohen, R. E., et al. 2023b, arXiv:2307.08738
Minor, Q. E., Martinez, G., Bullock, J., Kaplinghat, M., & Trainor, R. 2010, ApJ, 721, 1142
Moore, B., Ghigna, S., Governato, F., et al. 1999, ApJL, 524, L19
Moskowitz, A. G., & Walker, M. G. 2020, ApJ, 892, 27
Muñoz, R. R., Carlin, J. L., Frinchaboy, P. M., et al. 2006, ApJL, 650, L51
Muñoz, R. R., Côté, P., Santana, F. A., et al. 2018, ApJ, 860, 66
Munshi, F., Brooks, A. M., Christensen, C., et al. 2019, ApJ, 874, 40
Mutlu-Pakdil, B., Sand, D. J., Carlin, J. L., et al. 2018, ApJ, 863, 25
Mutlu-Pakdil, B., Sand, D. J., Crnojević, D., et al. 2022, ApJ, 926, 77
Nadler, E. O., Drlica-Wagner, A., Bechtol, K., et al. 2021, PhRvL, 126, 091101
Nadler, E. O., Gluscevic, V., Driskell, T., et al. 2024, arXiv:2401.10318
Nadler, E. O., Wechsler, R. H., Bechtol, K., et al. 2020, ApJ, 893, 48
Navarro, J. F., Frenk, C. S., & White, S. D. M. 1997, ApJ, 490, 493
Nebrin, O., Giri, S. K., & Mellema, G. 2023, MNRAS, 524, 2290
Newton, O., Cautun, M., Jenkins, A., Frenk, C. S., & Helly, J. C. 2018, MNRAS, 479, 2853
Newton, O., Leo, M., Cautun, M., et al. 2021, JCAP, 2021, 062
Pace, A. B. 2024, arXiv:2411.07424
Pace, A. B., Kaplinghat, M., Kirby, E., et al. 2020, MNRAS, 495, 3022
Pace, A. B., & Li, T. S. 2019, ApJ, 875, 77
Pace, A. B., & Strigari, L. E. 2019, MNRAS, 482, 3480
Pallanca, C., Leanza, S., Ferraro, F. R., et al. 2023, ApJ, 950, 138
Peñarrubia, J., Navarro, J. F., & McConnachie, A. W. 2008, ApJ, 673, 226
Pianta, C., Capuzzo-Dolcetta, R., & Carraro, G. 2022, ApJ, 939, 3
Placco, V. M., Frebel, A., Beers, T. C., & Stancliffe, R. J. 2014, ApJ, 797, 21
Plummer, H. C. 1911, MNRAS, 71, 460
Press, W. H., & Schechter, P. 1974, ApJ, 187, 425
Prochaska, J., Hennawi, J., Westfall, K., et al. 2020, JOSS, 5, 2308
Richstein, H., Kallivayalil, N., Simon, J. D., et al. 2024, ApJ, 967, 72
Richstein, H., Patel, E., Kallivayalil, N., et al. 2022, ApJ, 933, 217
Ricotti, M., Parry, O. H., & Gnedin, N. Y. 2016, ApJ, 831, 204
Rosenberg, A., Saviane, I., Piotto, G., Aparicio, A., & Zaggia, S. R. 1998, AJ, 115, 648
Rybizki, J., Green, G. M., Rix, H.-W., et al. 2022, MNRAS, 510, 2597
Sales, L. V., Wetzel, A., & Fattahi, A. 2022, NatAs, 6, 897
Sand, D. J., Mutlu-Pakdil, B., Jones, M. G., et al. 2022, ApJL, 935, L17
Schlafly, E. F., & Finkbeiner, D. P. 2011, ApJ, 737, 103
Schlegel, D. J., Finkbeiner, D. P., & Davis, M. 1998, ApJ, 500, 525
Schönrich, R., Binney, J., & Dehnen, W. 2010, MNRAS, 403, 1829
Sevilla-Noarbe, I., Bechtol, K., Carrasco Kind, M., et al. 2021, ApJS, 254, 24
Simon, J., Bechtol, K., Drlica-Wagner, A., et al. 2019, BAAS, 51, 409
Simon, J. D. 2018, ApJ, 863, 89
Simon, J. D. 2019, ARA&A, 57, 375
Simon, J. D., Drlica-Wagner, A., Li, T. S., et al. 2015, ApJ, 808, 95
Simon, J. D., & Geha, M. 2007, ApJ, 670, 313
Simon, J. D., Geha, M., Minor, Q. E., et al. 2011, ApJ, 733, 46
Simon, J. D., Li, T. S., Drlica-Wagner, A., et al. 2017, ApJ, 838, 11
Simon, J. D., Li, T. S., Erkal, D., et al. 2020, ApJ, 892, 137
Smith, S. E. T., Cerny, W., Hayes, C. R., et al. 2023a, arXiv:2311.10147
Smith, S. E. T., Cerny, W., Hayes, C. R., et al. 2024, ApJ, 961, 92
Smith, S. E. T., Jensen, J., Roediger, J., et al. 2023b, AJ, 166, 76
Sohn, S. T., Majewski, S. R., Muñoz, R. R., et al. 2007, ApJ, 663, 960
Somerville, R. S. 2002, ApJL, 572, L23
Spencer, M. E., Mateo, M., Olszewski, E. W., et al. 2018, AJ, 156, 257
Spencer, M. E., Mateo, M., Walker, M. G., & Olszewski, E. W. 2017, ApJ, 836, 202
Springel, V., Wang, J., Vogelsberger, M., et al. 2008, MNRAS, 391, 1685
Strader, J., & Kobulnicky, H. A. 2008, AJ, 136, 2102
Tan, C. Y., Cerny, W., Drlica-Wagner, A., et al. 2024, arXiv:2408.00865
Ting, Y.-S., Conroy, C., Rix, H.-W., & Cargile, P. 2019, ApJ, 879, 69
Torrealba, G., Belokurov, V., Koposov, S. E., et al. 2018, MNRAS, 475, 5085
Torrealba, G., Belokurov, V., & Koposov, S. E. 2019, MNRAS, 484, 2181
Torrealba, G., Koposov, S. E., Belokurov, V., & Irwin, M. 2016a, MNRAS, 459, 2370
Torrealba, G., Koposov, S. E., Belokurov, V., et al. 2016b, MNRAS, 463, 712
van der Walt, S., Colbert, S. C., & Varoquaux, G. 2011, CSE, 13, 22
Virtanen, P., Gommers, R., Oliphant, T. E., et al. 2020, NatMe, 17, 261
Walker, M. G., Mateo, M., Olszewski, E. W., et al. 2006, AJ, 131, 2114
Walker, M. G., Mateo, M., & Olszewski, E. W. 2009, AJ, 137, 3100
Walker, M. G., Mateo, M., Olszewski, E. W., et al. 2015a, ApJ, 808, 108
Walker, M. G., Olszewski, E. W., & Mateo, M. 2015b, MNRAS, 448, 2717
Wang, M. Y., de Boer, T., Pieres, A., et al. 2019, ApJ, 881, 118
Wang, W., Zhu, L., Jing, Y., et al. 2023, ApJ, 956, 91
Weerasooriya, S., Bovill, M. S., Benson, A., Musick, A. M., & Ricotti, M. 2023, ApJ, 948, 87
Weisz, D. R., Koposov, S. E., Dolphin, A. E., et al. 2016, ApJ, 822, 32
Wetzel, A. R., Deason, A. J., & Garrison-Kimmel, S. 2015, ApJ, 807, 49
Wetzel, A. R., Tinker, J. L., Conroy, C., & van den Bosch, F. C. 2013, MNRAS, 432, 336
Wheeler, A. J., Abruzzo, M. W., Casey, A. R., & Ness, M. K. 2023, AJ, 165, 68
Wheeler, A. J., Casey, A. R., & Abruzzo, M. W. 2024, AJ, 167, 83
Wheeler, C., Oñorbe, J., Bullock, J. S., et al. 2015, MNRAS, 453, 1305
White, S. D. M., & Frenk, C. S. 1991, ApJ, 379, 52
White, S. D. M., & Rees, M. J. 1978, MNRAS, 183, 341
Willman, B., Blanton, M. R., West, A. A., et al. 2005a, AJ, 129, 2692
Willman, B., Dalcanton, J. J., Martinez-Delgado, D., et al. 2005b, ApJL, 626, L85
Willman, B., Geha, M., Strader, J., et al. 2011, AJ, 142, 128
Willman, B., & Strader, J. 2012, AJ, 144, 76
Wolf, J., Martinez, G. D., Bullock, J. S., et al. 2010, MNRAS, 406, 1220
Zonca, A., Singer, L., Lenz, D., et al. 2019, JOSS, 4, 1298
Zucker, D. B., Belokurov, V., Evans, N. W., et al. 2006, ApJL, 650, L41